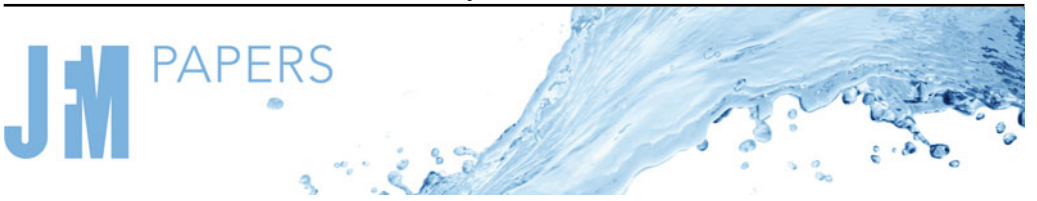
J. Fluid Mech. (2026), *vol.* 1039, A42, doi:10.1017/jfm.2026.11779



Investigating Rayleigh–Taylor instabilities using a statistically stationary and homogeneous simulation framework

Aaron Nelson[1] **and Guillaume Blanquart**[1]

[1]California Institute of Technology, Pasadena, CA 91125, USA

Corresponding author: Aaron Nelson, aanelson@caltech.edu

(Received 21 December 2025 UTC; revised 22 May 2026 UTC; accepted 29 May 2026 UTC)

Homogeneous buoyant turbulence (HBT) is developed as a novel direct numerical simulation (DNS) framework for modelling the small scales of turbulence in a temporally evolving Rayleigh–Taylor instability (TRT). Using a set of coordinate and variable transformations, statistical stationarity and homogeneity in all three directions are introduced to the TRT flow variables. These transformations produce a set of source terms in the governing equations, which, within a region surrounding the TRT midplane, reduce to just two non-negligible terms in the momentum and scalar transport equations. When applied to a periodic box domain, the new governing equations are verified to produce a stationary, homogeneous flow. Validation is performed for HBT against a large-scale TRT DNS, where probability density functions, the anisotropy of the kinetic energy and the anisotropy of the velocity gradient tensor are successfully reproduced. Turbulence spectra of HBT also show strong fidelity to the TRT spectra at the midplane, including the velocity and density spectra and the density–vertical velocity cospectrum. Significant computational savings are afforded by HBT compared to TRT DNS, owing to its smaller domain and shorter transient period. Furthermore, HBT's statistical stationarity and homogeneity facilitates the estimation of turbulence statistics to a high degree of precision. The framework has potential applications in the development of subgrid scale models for buoyant flows.

Key words: buoyancy-driven instability, homogeneous turbulence, turbulence simulation

1. Introduction

Turbulence arising from buoyant instabilities is a critical component in natural phenomena like underwater plumes, wildfire smoke and Type 1A supernovae. They also appear in engineering applications like inertial confinement fusion and scramjet combustors. A comprehensive list of examples can be found in the review article by Zhou (2017*a*). These

© The Author(s), 2026. Published by Cambridge University Press.

https://doi.org/10.1017/jfm.2026.11779 Published online by Cambridge University Press

Configuration	#HD	Stat.	Source of density variance
TRT (Cabot & Cook 2006)	2	No	Pure fluid reservoirs
Livescu (Livescu & Ristorcelli 2008)	3	No	Initial conditions
Chung (Chung & Pullin 2010)	2	Yes	Source terms in fringe regions
Carroll (Carroll & Blanquart 2015)	3	Yes	Numerical forcing terms
USH (Griffond *et al.* 2014)	3	No	Physics-derived source terms
SRT (Goh & Blanquart 2025)	2	Yes	Pure fluid reservoirs
HBT	3	Yes	Physics-derived source terms

Table 1. Configurations related to RT with representative studies (#HD, number of homogeneous directions; USH, unstably stratified homogeneous turbulence).

instabilities occur when an interface between two fluids of unequal densities is subject to an acceleration, either impulsive or continuous.

Cases where the applied acceleration is continuous are referred to as Rayleigh–Taylor (RT) instabilities. They were originally investigated by Rayleigh (1882) and Taylor (1950) as a linear stability problem. When the acceleration field is directed from the heavy fluid to the light, baroclinic torque causes disturbances in the interface to grow exponentially until nonlinear effects become dominant and a turbulent layer forms. Experimental (Dimonte & Schneider 2000; Ramaprabhu & Andrews 2004; Banerjee, Kraft & Andrews 2010) and computational (Youngs 1984; Zhou 2001; Ristorcelli & Clark 2004; Vladimirova & Chertkov 2009; Youngs 2013) studies of the turbulent layer have found an asymptotic tendency towards self-similar growth. In this limit, the height of the layer h evolves according to a differential equation of the form

$$\dot{h}^2 \propto h \tag{1.1}$$

where a variety of definitions have been used for h (a list is given in table 1 of Goh & Blanquart (2025)). The integral length scale scales with h and the turbulent velocity scales with $\dot{h}$. While the height of the layer grows, the Kolmogorov length scale η,

$$\eta = \left(\frac{\nu^3}{\widetilde{\epsilon}}\right)^{1/4}, \tag{1.2}$$

where ν is the kinematic viscosity and $\widetilde{\epsilon}$ is the Favre average of viscous dissipation, shrinks, such that the Reynolds number rises over time.

A review of RT research in general is given by Zhou (2017*a*,*b*). More specialized reviews in theoretical modelling (Abarzhi 2010), the Boussinesq limit (Boffetta & Mazzino 2017) and experiments (Andrews & Dalziel 2010; Banerjee 2020) also exist. Schilling (2020) provides a summary of efforts to integrate models, simulations and experiments.

1.1. *Computational challenges*

Practical RT flows are characterized by high Reynolds numbers, often combined with shocks, combustion and multiphase interactions. These complications make direct numerical simulations (DNS) prohibitively expensive to resolve. Large-eddy simulations (LES) could reduce the necessary resolution to a tractable level, but they require subgrid scale (SGS) models that accurately represent the unresolved turbulence. Unfortunately, only a few RT LES studies have used explicit SGS models (Mellado, Sarkar & Zhou 2005; Burton 2009; Yilmaz 2020; Luo *et al.* 2023); the others have relied on implicit LES (Dimonte *et al.* (2004) and references therein) or artificial fluid models (Cook, Cabot & Miller 2004). Among the SGS studies, only a few (Cook *et al.* 2004; Luo *et al.* 2023)

https://doi.org/10.1017/jfm.2026.11779 Published online by Cambridge University Press

have made attempts to validate against DNS results. Moreover, LES studies of related flows, such as buoyant plumes (Tieszen *et al.* 2002; DesJardin, O'Hern & Tieszen 2004) and buoyant wall-jets (Addad, Benhamadouche & Laurence 2004) have had difficulty predicting root-mean-square (r.m.s.) velocity and achieving grid independence. Novel SGS models, designed specifically to account for buoyant effects, are necessary before RT LES becomes reliable.

Performing DNS on the canonical planar RT configuration is one way to investigate the physics of RT instabilities without relying on intractable resolutions or unproven SGS models. In this configuration, hereafter referred to as temporally evolving Rayleigh–Taylor (TRT), the acceleration is constant, the domain is rectangular and the fluids are initially separated into two semi-infinite, uniform, quiescent reservoirs,

$$\rho(t=0, x_i) = \begin{cases} \rho_L, & x_1 < 0, \\ \rho_H, & x_1 > 0, \end{cases} \tag{1.3}$$

$$u_i(t=0, x_i) = 0, \tag{1.4}$$

where ρ is the density, u_i is the velocity and the H and L subscripts indicate properties of the heavy and light fluids. The flow can be characterized by three non-dimensional numbers: a Reynolds number,

$$Re = \frac{\dot{h}h}{\nu}; \tag{1.5}$$

an Atwood number,

$$At = \frac{\rho_H - \rho_L}{\rho_H + \rho_L}; \tag{1.6}$$

a Schmidt number,

$$Sc = \frac{\nu}{D}. \tag{1.7}$$

Here, ν is kinematic viscosity, and D is the scalar diffusivity. Some of the largest TRT DNS to date include the studies of Cabot & Cook (2006) (3072^3 grid points) and Livescu, Wei & Petersen (2011) ($4096^2 \times 4032$ grid points).

Though inexpensive compared with practical RT configurations, TRT suffers from computational drawbacks.

(i) Long simulation time. For a given target Reynolds number, the TRT must be run from the initial perturbations until the layer grows to the necessary height. This means that the bulk of the computational cost is spent on simulating a flow that is less turbulent than the regime of interest.

(ii) Growing domain size. Because the height of the RT layer grows with time, the final Reynolds number sets the required domain size for the overall simulation. Therefore, either the entire simulation must be run with the final computational grid, or the grid must evolve with time. The former approach over-resolves the flow at early times, and the latter approach introduces the non-trivial cost and complexity of an adaptive grid.

(iii) Statistical non-stationarity and inhomogeneity. Since the flow and its statistics evolve with time, the flow at the exact desired Reynolds number can only be observed over a short time window. Because the flow is homogeneous in only the two horizontal directions, an estimate of an ensemble average statistic can only be calculated

https://doi.org/10.1017/jfm.2026.11779 Published online by Cambridge University Press

from a single plane of grid points. Further data must be gathered from additional realizations, each requiring a new simulation starting from initial perturbations.

1.2. *Alternative configurations*

To circumvent one or more of the computational inefficiencies associated with TRT, alternative configurations have been proposed to capture the same physics at a reduced cost.

Livescu & Ristorcelli (2007) initialized random blobs of heavy and light fluid in a triply periodic box domain, then applied a constant gravitational field. This produced buoyancy-generated turbulence that is homogeneous in all three directions, allowing easier estimation of statistics. However, the turbulence still evolves continuously until the two fluids mix completely and the turbulence decays.

Chung & Pullin (2010) also used a triply periodic box with the same initialization, but added source and sink terms of density, active in fringe regions at the top and bottom (respectively) of the domain. These serve to counteract the turbulence decay in a manner analogous to fluid reservoirs, inducing a stationary buoyant flow. Averages can be taken over time, but not in the vertical spatial direction, which is inhomogeneous. The resulting flow is sensitive to the form of the source terms over much of the domain, so that relevant results are limited to a narrow slab around the horizontal midplane.

Carroll & Blanquart (2015) used a source term (active throughout the domain) to maintain the density variance in a triply periodic box. This source term is active everywhere, so that the flow is both stationary and homogeneous in all three directions. However, the term itself has no physical justification; it is questionable whether the generated density fluctuations are representative of real fluctuations in RT layers.

Griffond, Gréa & Soulard (2014) proposed another forced homogeneous scheme called unstably stratified homogeneous turbulence. Here, the governing equations have some physical justification, being a modified form of the Boussinesq equations for stably stratified turbulence (Godeferd & Cambon 1994). However, the framework assumes small density perturbations ($At \approx 0$). Furthermore, the flow fails to achieve stationarity, increasing in Reynolds number indefinitely.

Goh & Blanquart (2025) recently introduced a configuration called stationary Rayleigh–Taylor (SRT). In this framework, the TRT boundary conditions and fluid reservoirs are present, but the coordinates and velocity are rescaled to account for temporal evolution in the self-similar limit. The result resembles a statistically stationary version of the TRT configuration. The domain no longer grows with time, but homogeneity is still limited to two directions and a significant portion of the computational grid is still taken up by the reservoirs. The full SRT equations are reviewed in § 2.2.

1.3. *Homogeneous buoyant turbulence*

The properties of each of the discussed frameworks are summarized in table 1. All have succeeded in creating flows with some combination of three-dimensional homogeneity, stationarity and sources of density variance representative of TRT, but not all three at once.

To this end, the authors propose a novel configuration called homogeneous buoyant turbulence (HBT). The inspiration for this configuration is taken from the procedure of Rah, Dhandapani & Blanquart (2018). By adapting the reasoning used by Lundgren (2003) to derive his linear forcing term for homogeneous isotropic turbulence (HIT), Rah *et al.* (2018) isolated and modelled the small scales of turbulence at the centreline of a round incompressible jet. They began by defining a set of transformations of the flow variables

https://doi.org/10.1017/jfm.2026.11779 Published online by Cambridge University Press

to homogenize them at a specific location along the centreline. After substitution in the Navier–Stokes equations, evaluation at the target location and simplifications guided by an analysis of the kinetic energy budget, the authors obtained a new set of governing equations, identical to the original except for source terms in the momentum equations. When implemented in a triply periodic box domain, these source terms act to maintain the kinetic energy. The resulting stationary homogeneous flow was found to reproduce statistics (including turbulence spectra) observed in DNS of turbulent round jets. The same procedure was later applied to shear layers (Dhandapani, Rah & Blanquart 2019).

The objective of the present study is to use the same procedure to model the small scales of turbulence near the midplane of an RT instability. The result is a statistically stationary, fully homogeneous simulation framework for studying RT instabilities.

The paper is arranged thus: § 2 describes the derivation of the HBT governing equations, analogous to Rah *et al.* (2018). Section 3 discusses the closure of these equations and the non-dimensionalization of the simulation parameters. Section 4 describes the computational methods and lists the simulation cases. Sections 5 and 6 present the results, first a series of low-Reynolds number cases to elucidate numerical properties of the framework, then a few high Reynolds number cases to validate results against the TRT DNS performed by Cabot & Cook (2006). Finally, § 7 summarizes the computational benefits afforded by HBT and briefly addresses potential applications to turbulence model development.

2. Governing equations

The governing equations for HBT are derived in five steps. In § 2.1, the TRT governing equations are introduced. In § 2.2, variable transformations are substituted into the governing equations to achieve statistical stationarity. In § 2.3 further transformations are applied to approximate statistical homogeneity at the layer midplane. In § 2.4, these transformations are substituted into the stationary governing equations to derive a new set of equations. Finally, negligible terms are removed to produce the HBT governing equations in § 2.5.

Throughout the following discussion, an overline indicates a Reynolds (ensemble) average, $\overline{\phi}$, and a tilde indicates a Favre average, $\widetilde{\phi} = \overline{\rho\phi}/\overline{\rho}$. A prime and double prime indicate the corresponding fluctuations: $\phi' = \phi - \overline{\phi}$, $\phi'' = \phi - \widetilde{\phi}$.

2.1. *Governing equations for TRT*

The canonical RT configuration is governed by the low-Mach number, variable-density, Navier–Stokes equations with a single transported scalar,

$$\frac{\partial \rho}{\partial t} + \frac{\partial \rho u_j}{\partial x_j} = 0, \tag{2.1}$$

$$\frac{\partial \rho u_i}{\partial t} + \frac{\partial \rho u_i u_j}{\partial x_j} = -\frac{\partial p}{\partial x_i} + \frac{\partial \tau_{ij}}{\partial x_j} - (\rho - \overline{\rho}) g \delta_{1i}, \tag{2.2}$$

$$\frac{\partial \rho Y}{\partial t} + \frac{\partial \rho u_j Y}{\partial x_j} = \frac{\partial}{\partial x_j}\left(\rho D \frac{\partial Y}{\partial x_j}\right), \tag{2.3}$$

where ρ is the density, u_i is the ith component of velocity, p is the pressure, Y is the scalar, D is the diffusivity, g is the gravity and τ_{ij} is the viscous stress tensor, defined as

https://doi.org/10.1017/jfm.2026.11779 Published online by Cambridge University Press

$$\tau_{ij} = \rho\nu \left(\frac{\partial u_i}{\partial x_j} + \frac{\partial u_j}{\partial x_i} - \frac{2}{3}\frac{\partial u_k}{\partial x_k}\delta_{ij} \right), \tag{2.4}$$

where ν is the kinematic viscosity (assumed constant for this study) and δ_{ij} is the Kronecker delta. Einstein summation notation is used for the coordinate indices. Here, the hydrostatic component of the gravity, $-\overline{\rho} g \delta_{1i}$, has been absorbed into the pressure gradient, such that the pressure is uniform within each reservoir.

The four flow variables, u_i, ρ, p and Y, are determined by (2.1)–(2.3) and an equation of state (EoS) of the form

$$\rho = f(Y). \tag{2.5}$$

In the TRT configuration, the ideal gas EoS is used,

$$\rho = \frac{P_o W}{RT}, \tag{2.6}$$

where P_o is the spatially uniform background pressure, W is the mixture molecular weight and R is the universal gas constant. It is further assumed that variations in density can arise from either the molar mass $1/W = Y/W_L + (1-Y)/W_H$ or the temperature $T = YT_L + (1-Y)T_H$, but not both. The scalar Y represents either the mass fraction of the lighter fluid in a binary mixture or a non-dimensionalized temperature. In either case, the EoS can be written as

$$\rho = \frac{1}{\alpha Y + \beta} \tag{2.7}$$

where α and β are constant coefficients that can be chosen arbitrarily, provided the initial and boundary conditions of Y are consistent with those of ρ. For example, when the density is bounded between two limits, ρ_L and ρ_H, it is common to set $\alpha = 1/\rho_L + 1/\rho_H$ and $\beta = -1/\rho_H$ such that $0 \leqslant Y \leqslant 1$. However, it is more algebraically convenient in the context of this study to set $\beta = 0$ so that

$$\rho = \frac{1}{\alpha Y}, \tag{2.8}$$

and $1/(\alpha\rho_H) \leqslant Y \leqslant 1/(\alpha\rho_L)$. Here α can also be set to a value of 1 for convenience, but it is retained symbolically in the analysis for dimensional consistency.

The canonical RT configuration initializes these equations with two reservoirs of heavy/light fluid separated by a disturbed planar interface. This produces a flow that is statistically homogeneous and isotropic in the two horizontal directions, but neither homogeneous nor isotropic vertically. The height of the resulting mixing layer grows indefinitely, so that statistical stationarity is never achieved.

2.2. *Variable transformations for stationarity*

Recently, Goh & Blanquart (2025) proposed a modification to the TRT governing equations to simulate the RT instability in a statistically stationary framework. Their work relies on a rescaling of the variables according to the expected growth of velocity scales and length scales in the self-similar limit:

$$t^\dagger = t, \quad x_1^\dagger = \frac{h_0}{h(t)} x_1, \quad x_2^\dagger = x_2, \quad x_3^\dagger = x_3, \tag{2.9}$$

$$\rho^\dagger = \rho, \quad u_i^\dagger = u_i \frac{\dot{h}_0}{\dot{h}(t)}, \quad Y^\dagger = Y, \quad \frac{\partial p^\dagger}{\partial x_i^\dagger} = \frac{\partial p}{\partial x_i}, \tag{2.10}$$

https://doi.org/10.1017/jfm.2026.11779 Published online by Cambridge University Press

where h is any measure of the mixing height, and h_o is its value at an arbitrary time $t = t_o$. Although the horizontal coordinates scale with the layer height as well, they are not rescaled in the transformations to preserve horizontal homogeneity. In SRT, this causes horizontal length scales to grow until confined by the periodic boundary conditions. Nonetheless, the successful validation of SRT against TRT by Goh & Blanquart (2025) indicates that the confined horizontal scales behave analogously to a rescaling of the TRT horizontal scales.

The full form of the governing (2.1)–(2.3) with the substitutions of (2.9) and (2.10) are given in Goh & Blanquart (2025). They are omitted here for brevity. The full rescaled equations are still not stationary, since the Reynolds number will continue to increase as the Kolmogorov length scales shrink. To induce stationarity, Goh & Blanquart (2025) introduces the following three assumptions:

(i) the governing equations evaluated at $h(t) = h(t_0)$ are valid for a window of time centred at $t = t_0$ and longer than the integral time scale;
(ii) within this window, ensemble-averaged quantities are approximately constant, i.e. $\partial(\bar{\cdot})/\partial t^\dagger \approx 0$;
(iii) within this window, $h(t)$ exhibits self-similar growth, as in (1.1).

With these assumptions, the equations simplify to

$$\frac{\partial \rho^\dagger}{\partial t} + \frac{\partial \rho^\dagger u_j^\dagger}{\partial x_j^\dagger} = R_\rho, \tag{2.11}$$

$$\frac{\partial \rho^\dagger u_i^\dagger}{\partial t^\dagger} + \frac{\partial \rho^\dagger u_i^\dagger u_j^\dagger}{\partial x_j^\dagger} = -\frac{\partial p^\dagger}{\partial x_i^\dagger} + \frac{\partial \tau_{ij}^\dagger}{\partial x_j^\dagger} - (\rho^\dagger - \overline{\rho^\dagger}) g \delta_{1i} + T_u + R_{u_i}, \tag{2.12}$$

$$\frac{\partial \rho^\dagger Y^\dagger}{\partial t} + \frac{\partial \rho^\dagger u_j^\dagger Y^\dagger}{\partial x_j^\dagger} = \frac{\partial}{\partial x_j^\dagger}\left(\rho^\dagger D \frac{\partial Y^\dagger}{\partial x_j^\dagger}\right) + R_Y, \tag{2.13}$$

where

$$\tau_o = \frac{h(t_o)}{\dot{h}(t_o)} \tag{2.14}$$

is the instantaneous time scale of the self-similar growth,

$$R_\rho = \frac{x_1^\dagger}{\tau_o}\frac{\partial \rho^\dagger}{\partial x_1^\dagger}, \quad R_{u_i} = \frac{x_1^\dagger}{\tau_o}\frac{\partial \rho^\dagger u_i^\dagger}{\partial x_1^\dagger}, \quad R_Y = \frac{x_1^\dagger}{\tau_o}\frac{\partial \rho^\dagger Y^\dagger}{\partial x_1^\dagger} \tag{2.15}$$

are source terms associated with the vertical length rescaling, and

$$T_{u_i} = -\frac{1}{2\tau_o}\rho^\dagger u_i^\dagger \tag{2.16}$$

is a source term associated with the velocity rescaling. The coordinate system is chosen such that $x_1^\dagger = 0$ corresponds to the midplane, the location about which the self-similar growth occurs. This coincides with the location of the initial interface between the fluid reservoirs and the location where $\partial(\overline{\rho^\dagger u_1^\dagger})/\partial x_1^\dagger = 0$.

Throughout the study, SRT data from Goh & Blanquart (2025) will be referenced as cases G1–G6, and SRT data from Goh *et al.* (2026) will be referenced as cases A01, A2,

https://doi.org/10.1017/jfm.2026.11779 Published online by Cambridge University Press

Case	Re_t	At	At_{eff}
G1	50	0.5	0.27
G2	130	0.5	0.25
G3	240	0.5	0.24
G4	350	0.5	0.23
G5	990	0.5	0.23
G6	1880	0.5	0.23
A01	360	0.01	0.004
A2	370	0.2	0.09
A5	360	0.5	0.24
A8	290	0.8	0.44

Table 2. List of SRT simulation cases from Goh & Blanquart (2025) and Goh *et al.* (2026). Output parameters are evaluated at midplane. For all cases, $Sc = 1$.

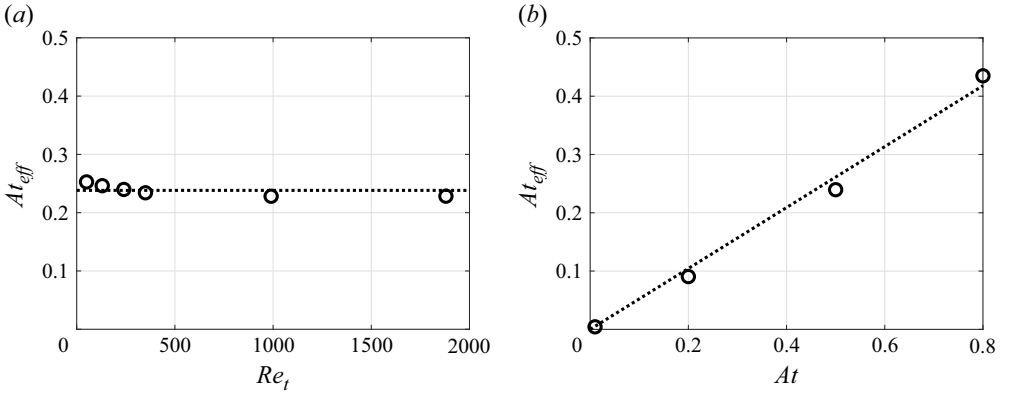


Figure 1. Midplane values of $At_{eff} = \rho_{rms}/\overline{\rho}$ versus (*a*) Re_t at the midplane for cases G1–6 of Goh & Blanquart (2025), with horizontal line indicating mean value, and (*b*) $At = (\rho_H - \rho_L)/(\rho_H + \rho_L)$ for cases {A01, A2, A5, A8} of Goh *et al.* (2026), with linear fit.

A5 and A8. Their corresponding Atwood number and midplane statistics are given in table 2. These statistics include the turbulent Reynolds number

$$Re_t = \frac{\widetilde{k}^2}{\widetilde{\epsilon}\nu}, \tag{2.17}$$

where $k = u_i^2/2$ is the kinetic energy and $\epsilon = \tau_{ij}(\partial u_i/\partial x_j)$ is the viscous dissipation, and an effective local Atwood number

$$At_{eff} = \frac{\overline{\rho'^2}^{1/2}}{\overline{\rho}}. \tag{2.18}$$

The relationship between $At_{eff}|_{x_1=0}$ and At in TRT can be inferred from SRT data. Figure 1(*a*,*b*) shows $At_{eff}|_{x_1=0}$ plotted against both $Re_t|_{x_1=0}$ and At for SRT cases. Here $At_{eff}|_{x_1=0}$ is nearly constant with respect to Reynolds number and almost linear with At. Therefore $At_{eff}|_{x_1=0}$ is a valid one-to-one metric for At.

https://doi.org/10.1017/jfm.2026.11779 Published online by Cambridge University Press

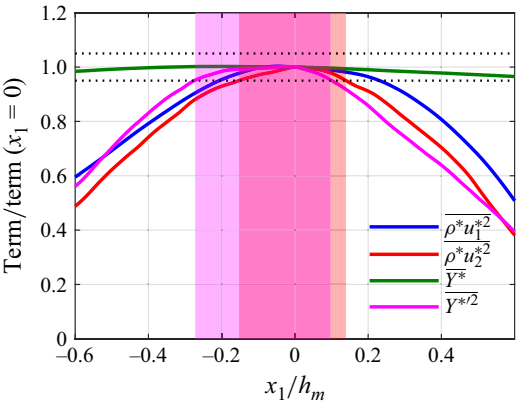


Figure 2. Averages over time and horizontal coordinates from SRT data (case G4). The vertical coordinate is normalized by the layer height as defined by Goh & Blanquart (2025), and statistics are normalized by their midplane values. The orange and purple shaded areas represent the regions where $\overline{\rho^* u_2^{*2}}$ and $\overline{Y^{*\prime 2}}$ are within 5 % of their midplane values, respectively.

2.3. *Variable transformations for homogeneity*

The aim of the proposed framework is the simultaneous satisfaction of statistical homogeneity in horizontal directions, homogeneity in the vertical direction and stationarity in time. The original equations (see § 2.1) are horizontally homogeneous; the transformations and simplifications of § 2.2 introduce stationarity. A second variable transformation,

$$\rho^\dagger, u_i^\dagger, p^\dagger \rightarrow \rho^*, u_i^*, p^*, \tag{2.19}$$

is now sought to introduce vertical homogeneity.

The transformations of (2.19) only contain sufficient degrees of freedom to make three statistics exactly uniform while maintaining the form of the EoS. The statistics chosen are $\overline{\rho^*}$, $\overline{\rho^* u_1^*}$ and $\overline{p^*}$, leading to the transformations

$$\rho^* = \rho^\dagger \frac{\overline{\rho_o^\dagger}}{\overline{\rho^\dagger}}, \quad u_i^* = (u_i^\dagger - \widetilde{u_1^\dagger}\delta_{1i}) \left(\frac{\overline{\rho^\dagger}}{\overline{\rho_o^\dagger}} \right)^{1/2}, \quad p^* = p^\dagger - \overline{p^\dagger}, \quad Y^* = \frac{\overline{\rho^\dagger}}{\overline{\rho_o^\dagger}} Y^\dagger. \tag{2.20}$$

The 'o' subscript implies evaluation at the midplane. Here $\overline{\rho^*}$ is homogenized by normalizing $\rho^\dagger$ by its ensemble average, while $\overline{\rho^* u_1^*} = \overline{\rho^*}\widetilde{u_1^*}$ and $\overline{p^*}$ are homogenized by subtracting the corresponding mean values from $u_i^\dagger$ and $p^\dagger$. The transformation for Y^* is defined to maintain the form of the EoS.

Although the transformations (2.20) homogenize exactly only three statistics, they induce approximate uniformity in a number of other statistics in the region surrounding the midplane. This is illustrated in figure 2. For the G4 SRT case, four statistics of the transformed variables are shown across the vertical coordinate: $\overline{\rho^* u_1^{*2}}$, $\overline{\rho^* u_2^{*2}}$, $\overline{Y^*}$ and $\overline{Y^{*\prime 2}}$. The first three of these remains within 5 % of their respective midplane value over a region of length $\approx 0.3 h_m$ centred at the midplane, where h_m is the definition of the layer height used by Goh & Blanquart (2025),

https://doi.org/10.1017/jfm.2026.11779 Published online by Cambridge University Press

Statistic	$2H/h_m$	$2H/l_1^\dagger$
$\overline{\rho^* u_1^{*2}}$	0.41	0.24
$\overline{\rho^* u_2^{*2}}$	0.28	0.17
$\overline{Y^*}$	1.61	0.96
$\overline{Y^{*\prime 2}}$	0.20	0.12

Table 3. Size of homogeneity region about the midplane for statistics in the G4 SRT case, as measured by the minimum distance H from the midplane where a statistic deviates by more than 5 % from its midplane value.

$$h_m = \frac{4(\rho_H + \rho_L)}{\rho_H \rho_L} \int \langle \rho Y(1-Y) \rangle_{2\text{-D}} \mathrm{d}x_1, \tag{2.21}$$

and $\langle \cdot \rangle_{2D}$ indicates a horizontal planar average. Note that the bounds of this region of homogeneity may not hold at higher Atwood number (i.e. greater than 0.5), where the peaks of these and other statistics shift towards the light fluid side of the layer (Goh *et al.* 2026). This effect is already apparent at $At = 0.5$ in the $\overline{Y^{*\prime 2}}$ profile of figure 2. Though more than $0.34h_m$ in width, the centre of its region of homogeneity is shifted to the left of the midplane by $\approx 0.08h_m$.

Table 3 gives values for the minimum distance H from the midplane where each statistic is greater than 5 % from its midplane value, multiplied by 2. This represents the maximum width of a region centred on the midplane where the statistic can be said to be homogeneous. Thus, HBT can be expected to model accurately TRT length scales at or below this metric.

The distances are normalized by both h_m and the characteristic vertical length scale $l_1^\dagger$. The latter is defined in terms of the vertical longitudinal correlation length,

$$l_1^\dagger = 2\pi \Lambda_1^\dagger = 2\pi \int C_1^\dagger(r)\mathrm{d}r, \quad C_1^\dagger(r) = \frac{\left\langle u_1^{\dagger\prime}(t^\dagger, x_1^\dagger + r, x_2^\dagger, x_3^\dagger) u_1^{\dagger\prime}(t, x_1^\dagger, x_2^\dagger, x_3^\dagger) \right\rangle_{2\text{-D}}}{\left\langle u_1^{\dagger\prime 2} \right\rangle_{2\text{-D}}}, \tag{2.22}$$

previously used by Zhou & Cabot (2019) for analysis of TRT and Goh & Blanquart (2025) for analysis of SRT. While the homogeneous region of $\overline{Y^*}$ spans more than one layer height and nearly one $l_1^\dagger$, the others only span a fraction of h_m and less than 20 % of $l_1^\dagger$. These regions may become even smaller at higher At as the profiles shift downwards. Nonetheless, $\kappa \geqslant 2\pi/0.12l_1$ represents a sizable portion of the turbulence length scales, and $At \leqslant 0.5$ accounts for most RT problems of practical relevance. Moreover, the quantitative comparison in § 6.3 will show that the turbulence spectra of HBT reproduce TRT spectra at scales well above the limits indicated by table 3.

While homogeneity is satisfied either exactly or approximately for several key statistics, some statistics remain inhomogeneous even at low Atwood number. These include the turbulent flux of kinetic energy $\overline{\rho^* u_1^* u_i^{*2}}$, the pressure flux of kinetic energy $\overline{u_1^* p^*}$ and the turbulent flux of scalar variance $\overline{u_1^{*\prime} Y^{*\prime 2}}$. Unfortunately, the degrees of freedom afforded by the variable transformations do not permit the homogenization of these fluxes. This is accepted as an inevitable source of error in the formulation. The impact of these inhomogeneities on the kinetic energy and scalar variance budgets are addressed in § 2.5.

https://doi.org/10.1017/jfm.2026.11779 Published online by Cambridge University Press

2.4. *Source terms*

From the transformations proposed in the previous section, the inverse transformations can be obtained:

$$\rho^\dagger = \frac{\overline{\rho^\dagger}}{\overline{\rho_o^\dagger}}\rho^*, \quad u_i^\dagger = \left(\frac{\overline{\rho_o^\dagger}}{\overline{\rho^\dagger}}\right)^{1/2} u_i^* + \widetilde{u_1^\dagger}\delta_{1i}, \quad p^\dagger = p^* + \overline{p^\dagger}, \quad Y^\dagger = \frac{\overline{\rho_o^\dagger}}{\overline{\rho^\dagger}}Y^*. \tag{2.23}$$

These transformations are now substituted into the governing equations for SRT. In the subsequent discussion, all variables not marked with an asterisk are presumed to carry the dagger superscript, which is omitted to save space.

At the same time, we leverage the exact and approximate homogeneity induced by the transformations to apply the following assumption:

(i) for a horizontal slab centred vertically at $x_1 = 0$, ensemble-averaged quantities of starred variables are approximately uniform, i.e. $\partial(\bar{\cdot})/\partial x_1 \approx 0$.

We also introduce the following two assumptions, which simplify the final equations:

(ii) within this slab, the governing equations evaluated at $\overline{\rho}(x_1) = \overline{\rho}(0)$, $\overline{\rho u}_1(x_1) = \overline{\rho u}_1(0)$, $(\mathrm{d}\overline{\rho}/\mathrm{d}x_1)(x_1) = (\mathrm{d}\overline{\rho}/\mathrm{d}x_1)(0)$ and $(\mathrm{d}\overline{\rho u_1}/\mathrm{d}x_1)(x_1) = (\mathrm{d}\overline{\rho u_1}/\mathrm{d}x_1)(0) = 0$ are valid;

(iii) within this slab, R_ρ, R_{u_i} and R_Y source terms arising from the stationarity transformations, being proportional to x_1, are negligible.

Starting with continuity (2.11),

$$\frac{\partial}{\partial t}\left(\frac{\overline{\rho}}{\overline{\rho}_o}\rho^*\right) + \frac{\partial}{\partial x_j}\left\{\left[\frac{\overline{\rho}}{\overline{\rho}_o}\rho^*\right]\left[\left(\frac{\overline{\rho}_o}{\overline{\rho}}\right)^{1/2} u_j^* + \widetilde{u}_1\delta_{1j}\right]\right\} = R_\rho. \tag{2.24}$$

Applying assumption (iii) and rearranging gives

$$\frac{\partial}{\partial t}\left(\frac{\overline{\rho}}{\overline{\rho}_o}\rho^*\right) + \frac{\partial}{\partial x_j}\left[\left(\frac{\overline{\rho}}{\overline{\rho}_o}\right)^{1/2}\rho^* u_j^*\right] + \frac{\partial}{\partial x_1}\left(\frac{\overline{\rho}}{\overline{\rho}_o}\rho^*\widetilde{u}_1\right) = 0. \tag{2.25}$$

This is then expanded to yield

$$\frac{\rho^*}{\overline{\rho}_o}\frac{\partial\overline{\rho}}{\partial t} + \frac{\overline{\rho}}{\overline{\rho}_o}\frac{\partial\rho^*}{\partial t} + \left(\frac{\overline{\rho}}{\overline{\rho}_o}\right)^{1/2}\left(\frac{\partial\rho^* u_j^*}{\partial x_j} + \frac{1}{2\overline{\rho}}\frac{\partial\overline{\rho}}{\partial x_1}\rho^* u_1^*\right) + \frac{\overline{\rho}}{\overline{\rho}_o}\left(\widetilde{u}_1\frac{\partial\rho^*}{\partial x_1} + \frac{\rho^*}{\overline{\rho}}\frac{\partial\overline{\rho}\widetilde{u}_1}{\partial x_1}\right) = 0. \tag{2.26}$$

Leveraging statistical stationarity and applying assumption (ii) leads to

$$\frac{\partial\rho^*}{\partial t} + \widetilde{u}_{1o}\frac{\partial\rho^*}{\partial x_1} + \frac{\partial\rho^* u_j^*}{\partial x_j} + \frac{1}{2\overline{\rho}_o}\frac{\mathrm{d}\overline{\rho}}{\mathrm{d}x_1}\bigg|_{x_1=0}\rho^* u_1^* = 0. \tag{2.27}$$

Performing a Galilean frame shift where $(\mathrm{D}/\mathrm{D}t) = (\partial/\partial t) + \widetilde{u}_{1o}(\partial/\partial x_1)$ further simplifies the equation. By assumption (i), the starred variables are statistically homogeneous, so this frame shift has no effect on the flow statistics. The transformed continuity equation is then

$$\frac{\mathrm{D}\rho^*}{\mathrm{D}t} + \frac{\partial\rho^* u_j^*}{\partial x_j} = S_\rho, \tag{2.28}$$

https://doi.org/10.1017/jfm.2026.11779 Published online by Cambridge University Press

which contains the additional source term

$$S_\rho = -\frac{\rho^* u_1^*}{2\lambda_o} \tag{2.29}$$

where

$$\lambda_o = \left(\frac{1}{\overline{\rho}_o} \frac{\mathrm{d}\overline{\rho}}{\mathrm{d}x_1}\bigg|_{x_1=0} \right)^{-1} \tag{2.30}$$

is a characteristic length scale associated with the density variation and mixing layer height.

To disentangle the evolution of density from that of the other primitive flow variables, the momentum (2.12) is first rewritten in its advective form, and assumption (iii) is applied to remove R_{u_i}:

$$\frac{\partial u_i}{\partial t} + u_j \frac{\partial u_i}{\partial x_j} = \frac{1}{\rho}\left(-\frac{\partial p}{\partial x_i} + \frac{\partial \tau_{ij}}{\partial x_j} + g(\rho - \overline{\rho})\delta_{i1} - \frac{1}{2\tau_o}\rho u_i \right). \tag{2.31}$$

Following a similar procedure as for the continuity equation, the momentum equation becomes

$$\frac{\mathrm{D}u_i^*}{\mathrm{D}t} + u_j^* \frac{\partial u_i^*}{\partial x_j} = \frac{1}{\rho}\left(-\frac{\partial p^*}{\partial x_i} + \frac{\partial \tau_{ij}^*}{\partial x_j} + g(\rho^* - \overline{\rho^*})\delta_{i1} - \frac{1}{2\tau_o}\rho^* u_i^* \right) + S_{u_i} \tag{2.32}$$

and the source term is

$$S_{u_i} = -\frac{1}{\rho^*}\frac{\mathrm{d}\overline{p}}{\mathrm{d}x_1} + \frac{1}{\rho^*}\frac{\partial \tau_{ij} - \tau_{ij}^*}{\partial x_j} - \frac{\widetilde{u}_1}{2\tau_o}\delta_{1i} + \frac{1}{\lambda_o}\left[\frac{u_1^* u_i^*}{2} + \frac{\widetilde{u}_1 u_i^*}{2} + \left(\widetilde{u}_1 u_1^* + \widetilde{u}_1^2 \right)\delta_{1i} \right] \tag{2.33}$$

where τ_{ij}^* is defined in the same way as its unstarred counterpart τ_{ij} in (2.4) but with the corresponding transformed flow variables.

Finally, the scalar equation transforms to

$$\frac{\mathrm{D}Y^*}{\mathrm{D}t} + u_j^* \frac{\partial Y^*}{\partial x_j} = \frac{1}{\rho^*}\frac{\partial}{\partial x_j}\left(\mathrm{D}\rho^* \frac{\partial Y^*}{\partial x_j} \right) + S_Y \tag{2.34}$$

with the source term

$$S_Y = -\mathrm{D}Y^* \frac{\partial}{\partial x_j}\left(\frac{1}{\overline{\rho}}\frac{\partial \overline{\rho}}{\partial x_1} \right) + \frac{1}{\lambda_o}\left(u_1^* Y^* + \widetilde{u}_1 Y^* \right). \tag{2.35}$$

To be used in the present numerical framework, the advective (2.32) and (2.34) must be converted back to conservative form,

$$\frac{\mathrm{D}\rho^* u_i^*}{\mathrm{D}t} + \frac{\partial \rho^* u_j^* u_i^*}{\partial x_j} = -\frac{\partial p^*}{\partial x_i} + \frac{\partial \tau_{ij}^*}{\partial x_j} + g\rho^{*'}\delta_{i1} - \frac{1}{2\tau_o}\rho^* u_i^* + \rho^* S_{u_i} + u_i^* S_\rho, \tag{2.36}$$

$$\frac{\mathrm{D}\rho^* Y^*}{\mathrm{D}t} + \frac{\partial \rho^* u_j^* Y^*}{\partial x_j} = \frac{\partial}{\partial x_j}\left(\mathrm{D}\rho^* \frac{\partial Y^*}{\partial x_j} \right) + \rho^* S_Y + Y^* S_\rho, \tag{2.37}$$

where S_ρ has entered through application of continuity (2.28).

While (2.28) and (2.36) are independent of the EoS, the EoS enters into the derivation of (2.37) twice. First, the transformation $Y \to Y^*$ in (2.20) is defined in terms of the general

https://doi.org/10.1017/jfm.2026.11779 Published online by Cambridge University Press

EoS, $\rho = f(Y)$, as

$$Y^* = f^{-1}\left(\frac{\overline{\rho}_o}{\overline{\rho}} f(Y)\right). \tag{2.38}$$

Second, after the transformations (2.20) are substituted into the original transport equation, the EoS is used to simplify the resulting equation to (2.37). The source terms that appear in the final transformed equation cannot be predicted universally, and can only be derived for a given EoS by defining the function $f(Y)$ and repeating the full derivation.

2.5. *Simplifications*

Equations (2.28), (2.36) and (2.37), with the EoS (2.8), govern the transformed flow variables near the midplane in SRT. Interestingly, many of the source terms added by the transformation have a relatively small impact on the flow and can be neglected. In this section, numerical SRT data will be surveyed across *Re* and *At* parameter space to determine which terms may be neglected.

The most obvious metric to assess the relative magnitude of each source term is the first moment of each equation. However, by definition of the transformed variables, the first moment of every term in the continuity equation is already zero. Similarly, the mean momentum and mean scalar equations do not provide much insight. Since reproducing the turbulent dynamics of the fluctuations is the intent of the present work, we compare scalings and magnitudes of the second moments.

For the transformed continuity equation, we compare the following five r.m.s. quantities:

$$C_i = \overline{\left(\frac{\partial \rho^* u_i^*}{\partial x_i}\right)^2}^{1/2} \quad \forall\, i \in \{1,2,3\}, \quad C_4 = \overline{\left(\sum_{j=1}^{3} \frac{\partial \rho^* u_j^*}{\partial x_j}\right)^2}^{1/2}, \quad C_5 = \frac{1}{2\lambda_o}\overline{\left(\rho^* u_1^*\right)^2}^{1/2}, \tag{2.39}$$

where there is no sum on the i indices. Here C_1, C_2 and C_3 represent the r.m.s. of the transformed convective terms individually, C_4 the r.m.s. of the same terms summed together and C_5 the r.m.s. of the source term S_ρ. We include C_4 because the fluctuations of the individual derivatives in the convective term cancel to produce smaller fluctuations in the total divergence of $\rho^* u_i^*$. Since the first moment of each term is zero, the relative magnitude of C_5 represents the influence of the source term over the continuity relationship and the flow overall.

Figure 3 shows each quantity, normalized by C_1, measured at the midplane for SRT cases G1–4. Since they are statistically equivalent, C_2 and C_3 are averaged together. For each case, C_5 is significantly smaller than the other r.m.s. values. Its ratio with C_1 decreases approximately as $Re_t^{-1/2}$, a scaling predicted by the self-similarity analysis of Ristorcelli & Clark (2004), and increases linearly with *At*. Since C_5 is an order of magnitude less than all other terms for $Re_t > 200$, and scales with *At* in the same way as the next smallest term, C_4, the assumption that S_ρ is negligible in (2.28) is understood to be valid for $Re_t \geqslant 200$ and all $At \leqslant 0.8$. All RT flows of practical relevance fall in this regime.

To assess the momentum terms, the second moment of the conservative form of the momentum equation is used. The equation for kinetic energy $\overline{\rho^*}\widetilde{k^*} = \overline{\rho^*}\widetilde{u_i^{*2}}/2$ is obtained

https://doi.org/10.1017/jfm.2026.11779 Published online by Cambridge University Press

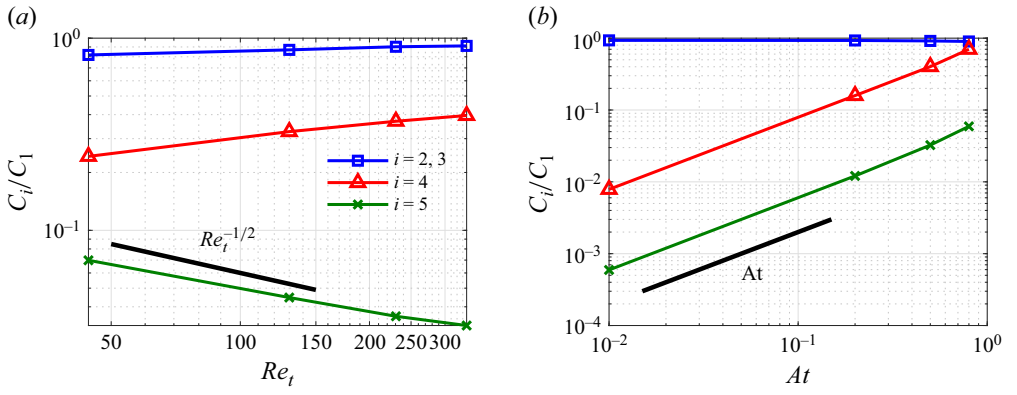


Figure 3. Quantities of (2.39), evaluated at midplane in SRT, plotted against (*a*) turbulent Reynolds number for cases G1–4 of Goh & Blanquart (2025) and (*b*) Atwood number for cases {A0, A2, A5, A8} of (Goh *et al.* 2026), normalized by C_1. Where i takes more than one value, the quantity is the average of the components with the corresponding indices.

by multiplying the momentum (2.36) by u^* and applying continuity:

$$\frac{D\overline{\rho^*}\widetilde{k^*}}{Dt} = \underbrace{-\frac{\partial \frac{1}{2}\overline{\rho^* u_i^{*2} u_j^*}}{\partial x_j} - \frac{\partial \overline{u_i^* p^*}}{\partial x_i}}_{I} \underbrace{+\overline{p^* \frac{\partial u_i^*}{\partial x_i}}}_{II} \underbrace{-\overline{\rho^*}\widetilde{\epsilon^*}}_{III} \underbrace{+\frac{\partial \overline{u_i^* \tau_{ij}^*}}{\partial x_j}}_{IV} \underbrace{+g\overline{\rho^{*\prime} u_1^{*\prime}}}_{V} \underbrace{-\frac{1}{2\tau_o}\overline{\rho^*}\widetilde{u_i^{*2}}}_{VI} + \overline{\rho^* u_i^* S_{u_i}} + \frac{1}{2}\overline{u_i^{*2} S_\rho}. \tag{2.40}$$

Using the definitions from (2.29) and (2.33), the source terms become

$$\overline{\rho^* u_i^* S_{u_i}} + \frac{1}{2}\overline{u_i^{*2} S_\rho} = \underbrace{-\overline{u_1^*}\frac{\mathrm{d}\overline{p}}{\mathrm{d}x_1}}_{VII} \underbrace{+\overline{u_i^* \frac{\partial \tau_{ij} - \tau_{ij}^*}{\partial x_j}}}_{VIII} \underbrace{+\frac{\widetilde{u}_1 \overline{\rho^*}\widetilde{k^*}}{\lambda_o}}_{IX} \underbrace{+\frac{\widetilde{u}_1 \overline{\rho^*}\widetilde{u_1^{*2}}}{\lambda_o}}_{X} \underbrace{+\frac{\overline{\rho^* u_1^* u_i^{*2}}}{4\lambda_o}}_{XI}. \tag{2.41}$$

The terms of (2.40), evaluated at the midplane of SRT cases and normalized by buoyant production, are presented in figure 4(*a*) for varying Re_t. As mentioned earlier, the kinetic energy is not strictly homogeneous at the midplane, so the advective term within the material derivative (left-hand side) is not exactly zero. However, it is consistently less than 1 % of the buoyant production. Similarly, the pressure dilatation (II) and two source terms (IV and VIII) represent less than 1 % of the production term. These are omitted from figure 4(*a*,*b*) and are understood to be negligible. All remaining terms show little variation in Reynolds number. Figure 4(*b*) shows the midplane values of the kinetic energy budget terms at varying At. The dissipation, buoyant production and layer growth (terms III, V and VI) remain in nearly constant proportion at all At. Transport (I) decreases gradually with At, but not according to any apparent power law. The magnitudes of terms IX, X and XI increase from zero as At rises.

Term VII remains below 2 % of the buoyant production at all tested Re_t and At and is therefore neglected. While terms IX and XI reach 10 % of production for the highest Atwood case, they are less than 5 % of production across Reynolds number for $At \leqslant 0.5$. Furthermore, their magnitudes are similar and of opposite signs across the parameter space; their contributions are expected to cancel. Thus, terms IX and XI are also neglected.

https://doi.org/10.1017/jfm.2026.11779 Published online by Cambridge University Press

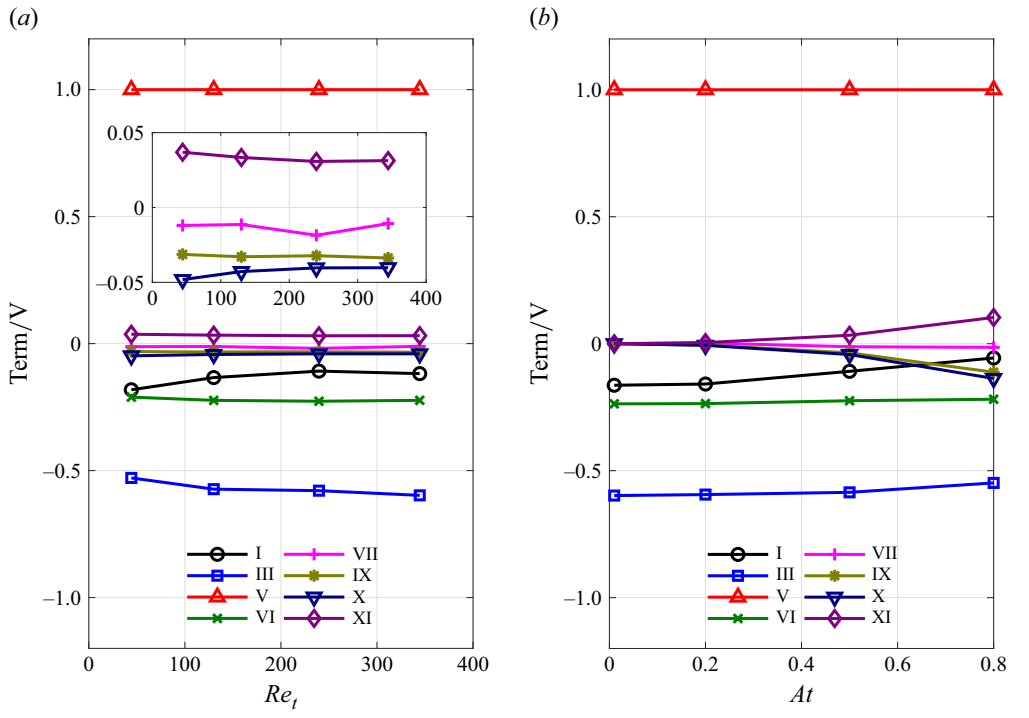


Figure 4. Terms in the transformed kinetic energy budget (2.40) evaluated at midplane versus (*a*) turbulent Reynolds number for cases G1–4 of Goh & Blanquart (2025) and (*b*) Atwood number for cases {A01, A2, A5, A8} of (Goh *et al.* 2026). Values are normalized by the term of largest magnitude. Terms with normalized absolute values consistently below 0.01 are omitted. The inset shows the same data in greater detail near the x-axis.

The dominant balance of the kinetic energy budget is between buoyant production (V), viscous dissipation (III), layer growth (VI), turbulent and pressure transport (I) and, at high At, the source term X. The transport term arises directly from inhomogeneity in the transformed turbulent flux of kinetic energy $\overline{\rho u_1^* u_i^{*2}}$ and the transformed pressure flux $\overline{u_1^* p^*}$. As discussed in § 2.3, this inhomogeneity is a consequence of the limited degrees of freedom available in defining the variable transformations (2.20). It is apparent from figure 4(*a*) that the increase in the magnitude of term X is nearly balanced by a decrease in the transport, so that summed together, these terms have a nearly constant contribution across Re_t and At. As a modelling closure, the buoyant production in HBT is reduced to account for the energy sink that these terms would otherwise provide. The implementation of this reduction is discussed further in § 3.1.

The scalar variance transport equation is derived by multiplying the advective form (2.34) of the scalar equation by $Y^{*'}$, then ensemble averaging,

$$\frac{D\overline{Y^{*'2}}}{Dt} = \underbrace{-\overline{u_1^*}\frac{\partial \overline{Y^{*'2}}}{\partial x_1}}_{I} \underbrace{-\frac{\partial \overline{u_1^{*'} Y^{*'2}}}{\partial x_1}}_{II} \underbrace{+2\overline{u_1^{*'} Y^{*'}}\frac{\partial \overline{Y^*}}{\partial x_1}}_{III} \underbrace{-2\overline{\chi}}_{IV} \underbrace{+D\frac{\partial^2 \overline{Y^{*'2}}}{\partial x_1^2}}_{V} \underbrace{+2D\overline{Y^{*'}\left(\frac{1}{\rho^*}\frac{\partial \rho^*}{\partial x_j}\frac{\partial Y^*}{\partial x_j}\right)}}_{VI} + 2\overline{Y^{*'} S_Y} \tag{2.42}$$

https://doi.org/10.1017/jfm.2026.11779 Published online by Cambridge University Press

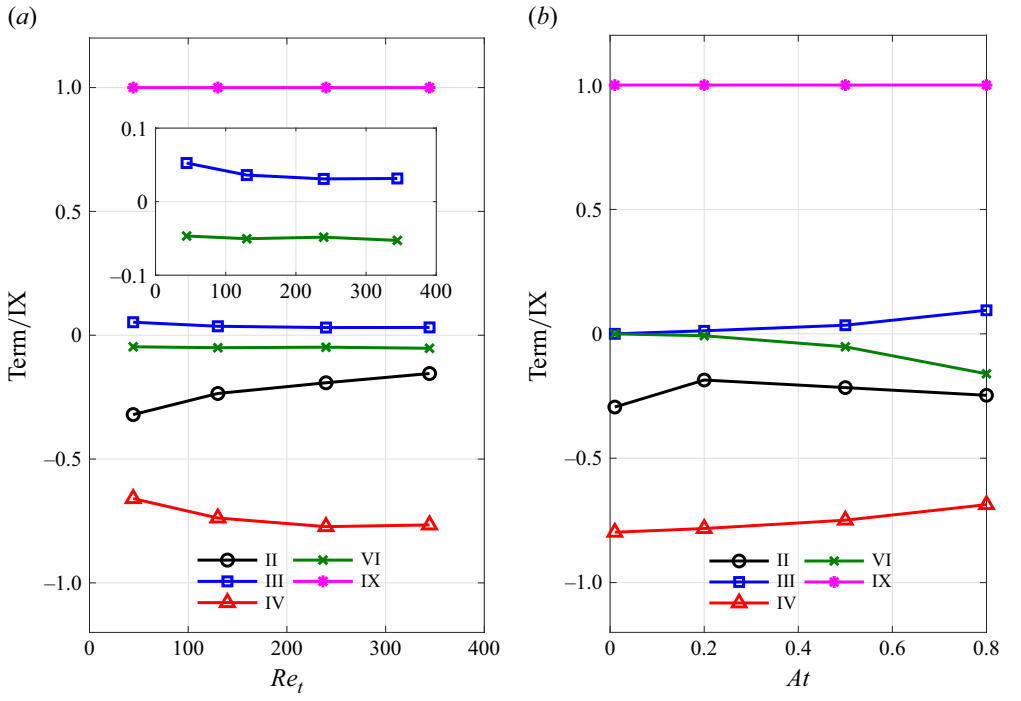


Figure 5. Terms in the transformed scalar variance budget (2.42) evaluated at midplane versus (*a*) turbulent Reynolds number for cases G1–4 of Goh & Blanquart (2025) and (*b*) Atwood number for cases {A0, A2, A5, A8} of (Goh *et al.* 2026). Values are normalized by the term of largest magnitude. Terms with normalized absolute values consistently below 0.01 are omitted. The inset shows the same data in greater detail near the *x*-axis.

where the scalar dissipation rate is

$$\chi = D\left(\frac{\partial Y^{*'}}{\partial x_j}\right)^2. \tag{2.43}$$

With the definition from (2.35), the source terms become

$$2\overline{Y^{*'}S_Y} = \underbrace{-2D\overline{Y^{*'2}}\frac{\partial}{\partial x_j}\left(\frac{1}{\overline{\rho}}\frac{\partial \overline{\rho}}{\partial x_1}\right)}_{VII} \underbrace{+2\frac{(\overline{u_1^*}+\widetilde{u}_1)\overline{Y^{*'2}}}{\lambda_o}}_{VIII} \underbrace{+2\frac{\overline{u_1^{*'}Y^{*'}Y^*}}{\lambda_o}}_{IX}. \tag{2.44}$$

The terms of the scalar variance budget are computed at the midplane of SRT and presented in figure 5(*a*) at varying Re_t. They are normalized by the mean gradient production. As in the kinetic energy equation, while the scalar variance is not strictly homogeneous at the midplane, the advective term in the material derivative is negligible (< 1 % of the production term). Similarly, terms I, V, VII and VIII are each less than 1 % of production and are omitted from the figure. The remaining terms are insensitive to Reynolds number. Figure 5(*b*) gives the midplane scalar variance budget terms at varying Atwood. The relative contributions of terms III and VI increase from zero as At rises. Notably, the decrease in the magnitude of term IV appears to balance the increase in term VI, while the decrease in term II is balanced by the increase in term III.

https://doi.org/10.1017/jfm.2026.11779 Published online by Cambridge University Press

The dominant balance is between the mean gradient production (XI), scalar dissipation (IV), turbulent transport (II) and a diffusive term arising from variation in density (VI), as well as the source term III at high Atwood. Like the pressure transport and turbulent transport of kinetic energy, the contribution to scalar variance by turbulent transport is a consequence of inhomogeneity in the transformed variables. The sum of terms II and III constitutes a variance sink that is nearly uniform across the parameter space, which is modelled in HBT by a reduction in the mean gradient production term, as discussed in § 3.1.

From the above analysis, the only term within the sources S_ρ, S_{u_i} and S_Y with a non-negligible contribution to continuity, kinetic energy transport or scalar variance transport is term IX in (2.44). The source terms therefore become

$$S_\rho \approx 0, \quad S_{u_i} \approx 0, \quad S_Y \approx \frac{u_1^{*'} Y^*}{\lambda_o}. \tag{2.45}$$

Substituting these into the transformed governing (2.28) and (2.36)–(2.37), the equations for HBT are now given by

$$\frac{\partial \rho^*}{\partial t} + \frac{\partial \rho^* u_j^*}{\partial x_j} = 0, \tag{2.46}$$

$$\frac{\partial \rho^* u_i^*}{\partial t} + \frac{\partial \rho^* u_i^* u_j^*}{\partial x_j} = -\frac{\partial p^*}{\partial x_i} + \frac{\partial \tau_{ij}^*}{\partial x_j} + g\rho^{*'}\delta_{1i} - \frac{1}{2\tau_o}\rho^* u_i^*, \tag{2.47}$$

$$\frac{\partial \rho^* Y^*}{\partial t} + \frac{\partial \rho^* Y^* u_j^*}{\partial x_j} = \frac{\partial}{\partial x_j}\left(\rho^* D \frac{\partial Y^*}{\partial x_j}\right) + \frac{u_1^{*'}}{\alpha \lambda_o}, \tag{2.48}$$

where the source term in the scalar equation has been simplified using the EoS (2.8). The mean gradient source term on the right-hand side of (2.48) acts to maintain the scalar variance, which in turn acts through the buoyancy term in (2.47) to maintain the kinetic energy.

It is interesting to note that (2.48) has the same form as the transport equation for temperature fluctuations in Rayleigh–Benard convection, where a mean temperature gradient is imposed. Seeing as the horizontally averaged scalar profile in an RT layer is approximately linear at the midplane, and inertial range scalings at the core of an RT mixing layer have been observed to be equivalent to those of Rayleigh–Benard convection in the two-dimensional (2-D) Boussinesq case (Mazzino 2017), it is not surprising that analogous flow dynamics emerge. The inclusion of $-(1/2\tau_o)\rho^* u_i^*$ in (2.47) to represent self-similar growth distinguishes HBT, a statistically stationary representation of a non-stationary flow, from Rayleigh–Benard convection, a statistically stationary flow.

3. Flow inputs for HBT

Aside from the initial and boundary conditions, running a simulation with the governing equations (2.46)–(2.48) requires knowledge of five parameters: ν, D, g, τ_o and λ_o. Constant values can be prescribed to ν and D as inputs. Sections 3.1 and 3.2 describe how the remaining variables are determined. Section 3.3 shows how non-dimensional groupings corresponding to the TRT non-dimensional parameters arise from the simulation inputs.

3.1. *Layer growth term*

The momentum equations in the HBT formulation (2.47) inherit one coefficient from the SRT formulation, the time scale τ_o. In the formulation of Goh & Blanquart (2025), it

https://doi.org/10.1017/jfm.2026.11779 Published online by Cambridge University Press

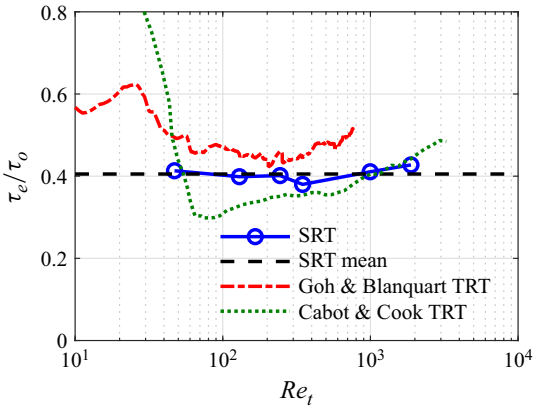


Figure 6. Measurements of τ_t/τ_o at midplane for SRT and TRT cases, versus the turbulent Reynolds number at midplane. Ensemble averages are approximated by averages across horizontal directions and, for SRT cases, time.

was identified with the inverse of the global average scalar dissipation rate over the entire mixing layer. Obviously, such a closure expression could not be extended to the HBT formulation. Nonetheless, other time scales are available in HBT which scale in the same manner as τ_o.

Since τ_o appears in the turbulent kinetic energy budget, and the goal of HBT is to reproduce the turbulence dynamics of SRT, it would be advantageous to relate τ_o to a time scale associated with the kinetic energy budget. The time scale chosen is the midplane value of the turbulence time scale $\tau_t = \widetilde{k}_o/\widetilde{\epsilon}_o$.

As established in § 2.2, τ_o models $h/\dot{h}$ in the corresponding TRT simulation. According to the scalings derived by Ristorcelli & Clark (2004), $h/\dot{h}$ scales with Re and At in the same way as τ_t in the self-similar limit. Therefore, τ_t and τ_o can be related to each other by a single non-dimensional constant across all values of Re and At. To evaluate this constant, τ_t/τ_o is measured over SRT cases G1–6 of Goh & Blanquart (2025). In figure 6, these measurements are plotted against the turbulent Reynolds number at the midplane. The TRT case T0 of Goh & Blanquart (2025) and the TRT data of Cabot & Cook (2006) are also shown for comparison, where $h_m/\dot{h}_m$ is used in place of τ_o. The SRT values appear to be constant across Reynolds number, confirming that τ_t and τ_o scale with Re_t in the same way. The six cases are averaged to yield $\tau_t/\tau_o \approx 0.41$. This average lies largely between the two TRT series, within 20 % of most of the data. In the HBT framework, the time scale τ_o is replaced by $\tau_t/0.41$. To compute τ_t numerically, the volume averages of turbulent kinetic energy and viscous dissipation rate are taken at each time step.

It is also noted that $\tau_t/\tau_o = (\widetilde{k}^*/\tau_o)/\widetilde{\epsilon}^*$, i.e. the ratio of the turbulence time scale and the layer growth time scale is equal to the ratio of the layer growth and viscous contributions to the kinetic energy budget (terms VI and III in (2.40)). Since the HBT budget is dominated by the buoyant production, viscous dissipation and layer growth, fixing the ratio between the latter two implies that any deviation in the balance of the HBT budget from TRT can be reduced to error in the magnitude of the production term. Thus, the terms neglected in § 2.5, such as the pressure and turbulent transport, emerge in HBT as a reduction in buoyant production. Likewise, since the scalar variance budget in HBT is dominated by just two terms, the neglected scalar variance budget terms emerge as a reduction in the mean gradient production.

https://doi.org/10.1017/jfm.2026.11779 Published online by Cambridge University Press

3.2. *Temporal fluctuation reduction*

The ability of (2.46)–(2.48) to produce turbulence in a homogeneous setting relies upon the presence of two source terms in the vertical velocity and scalar equations,

$$f_g = g\rho^{*'}, \quad f_\lambda = \frac{u_1^{*'}}{\alpha\lambda_o}, \tag{3.1}$$

representing the effects of gravity and the mean density gradient, respectively. Other source terms have been used to sustain HBT in previous studies (Soulard, Griffond & Gréa 2014; Carroll & Blanquart 2015). Unfortunately, like many homogeneous forcing methods (Eswaran & Pope 1988; Overholt & Pope 1998; Carroll & Blanquart 2013), these source terms produce statistics subject to large temporal fluctuations and correlations over long time scales. As a result, simulations must be run over long times to obtain time-averaged statistics within an acceptable degree of uncertainty. Shortening the required simulation time requires reducing either the correlation time scale or the fluctuation magnitude. While some stochastic forcing schemes (Eswaran & Pope 1988) permit the adjustment of the correlation time as an input parameter, it is undesirable to introduce stochasticity into a forcing term that is representative of a deterministic physical process. In the present work, measures are taken to reduce the temporal fluctuations instead.

Large, correlated fluctuations have also been identified (Carroll & Blanquart 2013) as a difficulty in the implementation of Lundgren (2003)'s linear forcing term,

$$f_L = Au_i, \tag{3.2}$$

where A is a constant forcing coefficient. The term appears in the momentum equation in the context of constant density turbulence:

$$\frac{\partial u_i}{\partial t} + u_j\frac{\partial u_i}{\partial x_j} = -\frac{\partial p}{\partial x_i} + \nu\frac{\partial 2u_i}{\partial x_j^2} + f_L. \tag{3.3}$$

If this equation is multiplied by u_i, the Reynolds average is taken and homogeneity is assumed, the kinetic energy equation is obtained as

$$\frac{\partial \overline{k}}{\partial t} = -\overline{\epsilon} + 2A\overline{k}. \tag{3.4}$$

If stationarity is further assumed, the following relationship results:

$$2A = \frac{\overline{\epsilon}}{\overline{k}} = \frac{1}{\tau_t}. \tag{3.5}$$

The forcing effectively induces the turbulence time scale τ_t time to approach $1/2A$ as the flow relaxes towards stationarity.

Initially proposed by Rosales & Meneveau (2005), Carroll & Blanquart (2013) explored the effects of a modification to the Lundgren forcing:

$$f_L^* = A\frac{k_o}{\langle k\rangle}u_i. \tag{3.6}$$

Here k_o is another constant, and the angle brackets indicate a volume-averaged quantity, which is a function of time only. The relationship of (3.5) becomes instead

$$2Ak_o = \overline{\epsilon} \tag{3.7}$$

so that the forcing coefficient determines the value of $\overline{\epsilon}$ rather than τ_t. In other words, $2Ak_o$ represents a prescribed constant rate of kinetic energy injection, which $\overline{\epsilon}$ must balance to maintain a stationary state.

https://doi.org/10.1017/jfm.2026.11779 Published online by Cambridge University Press

Carroll & Blanquart (2013) demonstrated that the modified source term (3.6) produces smaller fluctuations in $\langle k \rangle$ and $\langle \epsilon \rangle$ than the original source term (3.5). This was supported theoretically by a linear perturbation analysis, which suggests that the Lundgren forcing is only marginally stable for fluctuations in $\langle k \rangle$ and $\langle \epsilon \rangle$, whereas the modified Lundgren scheme damps the same fluctuations to smaller amplitudes.

To produce a similar effect, an analogous modification is proposed for the HBT forcing terms of (3.1). If the pressure dilatation is neglected, the kinetic energy equation for the HBT momentum (2.47) becomes

$$\frac{\partial \overline{\rho^*}\widetilde{k^*}}{\partial t} = -1.41\overline{\rho^*}\widetilde{\epsilon^*} + g\overline{\rho^{*'}u_1^{*'}}. \tag{3.8}$$

Stationarity then implies

$$g = -1.41\frac{\overline{\rho^*}\widetilde{\epsilon^*}}{\overline{\rho^{*'}u_1^{*'}}} \tag{3.9}$$

so that prescribing a value for g is equivalent to imposing the ratio of the viscous dissipation and the density–vertical velocity covariance. Likewise, the scalar variance equation becomes

$$\frac{\partial \overline{\rho^*}\widetilde{Y^{*''2}}}{\partial t} = -\overline{\rho^*}\widetilde{\chi^*} + \frac{\overline{u_1^{*'}Y^{*'}}}{\alpha\lambda_o}. \tag{3.10}$$

At stationarity this is

$$\frac{1}{\alpha\lambda_o} = \frac{\overline{\rho^*}\widetilde{\chi^*}}{\overline{u_1^{*'}Y^{*'}}}. \tag{3.11}$$

The ratio of the scalar dissipation and the vertical velocity-scalar covariance is imposed.

We propose to modify the original source terms (3.1) as follows:

$$f_g^* = -\overline{\rho^*}P_g\frac{\rho^{*'}}{|\langle \rho^{*'}u_1^{*'}\rangle|}, \quad f_\lambda^* = \overline{\rho^*}P_\lambda\frac{u_1^{*'}}{|\langle u_1^{*'}Y^{*'}\rangle|}. \tag{3.12}$$

The stationary relationships then become

$$P_g = 1.41\widetilde{\epsilon^*} \tag{3.13}$$

and

$$P_\lambda = \widetilde{\chi^*}. \tag{3.14}$$

Thus, the new source terms impose the values of $\widetilde{\epsilon^*}$ and $\widetilde{\chi^*}$ by injecting kinetic energy and scalar variance at prescribed average rates P_g and P_λ. A factor of 1.41 exists between the rate of kinetic energy injection and the viscous dissipation due to the presence of the layer growth term. The absolute values of the denominators are taken to ensure the modification does not change the sign of forcing during the initial transient. Data from all cases in this study have shown that the fluctuations of $\langle \rho^{*'}u_1^{*'}\rangle$ and $\langle u_1^{*'}Y^{*'}\rangle$ are only a small fraction of their mean values once a stationary state has been reached.

The source terms of (3.12) only differ from the original terms (3.1) by factors that are functions of time alone. The effect of the (3.12) modification on the temporal variation of HBT is investigated numerically in § 5.2.

https://doi.org/10.1017/jfm.2026.11779 Published online by Cambridge University Press

3.3. *Input non-dimensionalization*

The HBT governing (2.46)–(2.48) and EoS (2.8) require five inputs: the kinematic viscosity ν, the diffusivity D, gravity g, the characteristic length scale of density variation λ_o and the coefficient of the EoS α. If the modification (3.12) is used, g and λ_o are replaced as inputs by P_g and P_λ. The boundary conditions introduce a sixth input, the domain length L.

The statistics of the stationary flow are independent of the details of the initial flow field, as will be demonstrated in § 5.2. Taking the volume average of the continuity (2.46) over a triply periodic domain produces

$$\frac{\mathrm{d}\langle\rho\rangle}{\mathrm{d}t} = -\left\langle\frac{\partial\rho u_j}{\partial x_j}\right\rangle = 0 \tag{3.15}$$

where the second equality is due to the divergence theorem. The initial value of the volume average density is thus constant over the course of any simulation. It is therefore equivalent to the ensemble average $\overline{\rho}$, and constitutes a seventh input. The same might be said for the volume average momentum $\langle\rho u_i\rangle$ and scalar mass $\langle\rho Y\rangle$. However, $\langle\rho u_i\rangle$ is always set to zero, since it is only the velocity fluctuations that are of interest and not the mean flow, and $\langle\rho Y\rangle = 1/\alpha$ is just the coefficient of the EoS (2.8). As such, $\langle\rho u_i\rangle$ and $\langle\rho Y\rangle$ are not additional independent inputs in the present implementation.

In summary, the HBT configuration involves seven dimensional inputs: $\overline{\rho}$, ν, D, P_g, P_λ, L and α. Applying the Buckingham–Pi theorem with three dimensions (length, time, mass), the numerical solutions to the HBT equations may be characterized by $7-3=4$ non-dimensional groups. However, one of these is $\alpha\overline{\rho}$, which clearly has no impact on the dynamics of the flow beyond imposing a scale for the transported scalar Y. This leaves three groups to use as non-dimensional inputs for HBT.

The first of these is the Schmidt number, which can be defined in the same manner as the Schmidt number of TRT and SRT:

$$Sc_{HBT} = \frac{\nu}{D}. \tag{3.16}$$

The second group is the Reynolds number, which is constructed using $(P_g L)^{1/3}$ as a velocity scale and L as a length scale, taking the form

$$Re_{HBT} = \frac{L^{4/3}P_g^{1/3}}{\nu}. \tag{3.17}$$

The third non-dimensional group is akin to an Atwood number. Given the form of the new scalar (2.48) and the associated EoS (2.8), the density no longer has prescribed bounds ρ_L and ρ_H. Thus, the original Atwood definition of (1.6) cannot be used. Instead, it is defined as

$$At_{HBT} = \frac{\alpha\overline{\rho}P_\lambda^{1/2}L^{1/3}}{P_g^{1/6}}. \tag{3.18}$$

It will be shown in § 5.4 that this parameter scales with the magnitude of the relative density fluctuations, just as At does in TRT and SRT. The non-dimensional parameters given in (3.16), (3.17) and (3.18) uniquely characterize an HBT solution.

It is noted that

$$Re_t^*|_{x_1=0} \approx Re_t|_{x_1=0}, \quad At_{eff}^*|_{x_1=0} = At_{eff}|_{x_1=0}, \tag{3.19}$$

https://doi.org/10.1017/jfm.2026.11779 Published online by Cambridge University Press

in SRT. This is because, at the midplane of an SRT, $k^* = k$ and $\rho^* = \rho$. Additionally, since the term VIII in (2.41) is negligible, $\epsilon^* \approx \epsilon$. Therefore, an HBT simulation can be expected to resemble an SRT midplane, and by extension a TRT midplane, when the At^*_{eff} of Re^*_t of the HBT matches the $At_{eff}|_{x_1=0}$ and $Re_t|_{x_1=0}$ of the TRT.

Unfortunately, Re^*_t and At^*_{eff} cannot be calculated for an HBT simulation *a priori*. The relationship between these non-dimensional statistics and the non-dimensional inputs (3.17) and (3.18) is explored in § 5.4, and is used to produce HBT simulations targeting desired values of Re^*_t and At^*_{eff} in § 6.

4. Numerical implementation

4.1. *Numerical solver*

The finite difference solver NGA (Desjardins *et al.* 2008) is used to solve the conservative form of the HBT (2.46)–(2.48). The reader is referred to Desjardins *et al.* (2008) for full details of the numerical methods used; only a brief overview is provided below.

Second-order finite difference operators are used with variables stored on a staggered spatial grid. Higher-order discretizations are also possible within NGA, but a grid-sensitivity study found that second-order accuracy is sufficient to achieve grid convergence (see Appendix A). The vector and scalar quantities are also staggered in time. For time integration, a second-order semi-implicit iterative scheme is used with the fractional step method. The procedure is as follows: at each subiteration within a time step, the scalar (2.48) is advanced; then, the EoS (2.8) is enforced; the momentum (2.47) is advanced; finally, continuity (2.46) is enforced via a pressure projection step. As the iterations converge, the numerical framework approaches an implicit midpoint scheme.

Scalar transport is performed using the bounded cubic Hermite (BCH) scheme (Verma, Xuan & Blanquart 2014). The BCH scheme was found to incur less numerical diffusion compared with other bounded schemes, including the weighted essentially non-oscillatory (WENO) schemes (Xu & Shu 2005). Unfortunately, NGA guarantees primary conservation only when Eulerian time discretization is used, whereas BCH applies the scalar convection term through Lagrangian backtracing. As a result, BCH is subject to numerical errors in mass conservation. Over $40\tau_t$ of an HBT simulation, these can accumulate to a 10 % error in the mean density $\overline{\rho}$. To avoid this, a small spatially uniform correction is added to the scalar transport equation at each time step.

A slight conservation error is still present in the time integration, though this error vanishes with increasing numbers of subiterations. A more complete discussion of potential numerical errors and grid resolution effects is given in Appendix A.

The density and velocity fields are randomly initialized according to the procedure of Eswaran & Pope (1988), with three main deviations:

(i) the density field is initialized between the limits $0.9\overline{\rho} \leqslant \rho \leqslant 1.1\overline{\rho}$, rather than the scalar being initialized between $0 \leqslant Y \leqslant 1$;
(ii) the density field is shifted to satisfy exactly the input value for $\overline{\rho}$;
(iii) the velocity field is initialized via the analytical spectrum used by Rosales & Meneveau (2005) rather than through constant-density *a priori* simulations.

The reader is referred to Eswaran & Pope (1988) for further details.

4.2. *Simulation cases*

Table 4 gives a summary of the HBT simulation cases studied. Across all cases, the Schmidt number is set to 1. The dimensional parameters $\overline{\rho}$, L and P_g are held constant

https://doi.org/10.1017/jfm.2026.11779 Published online by Cambridge University Press

Case	Inputs				Outputs				M
	Re_{HBT}	At_{HBT}	N	# Subiter.	Re_t^*	At_{eff}^*	$\kappa_{max}\eta^*$	l/L	
K1	616	2.75	64	5	310	0.27	1.77	0.35	1
K2/S2	616	2.75	96	5	300	0.27	2.65	0.34	1
K3	616	2.75	128	5	300	0.27	3.54	0.35	1
K4	616	2.75	160	5	320	0.27	4.43	0.36	1
WK1	616	2.75	64	5	310	0.27	1.77	0.35	1
WK2/WS2	616	2.75	96	5	320	0.27	2.65	0.36	1
WK3	616	2.75	128	5	290	0.27	3.54	0.34	1
WK4	616	2.75	160	5	300	0.27	4.42	0.34	1
S1	616	2.75	96	3	290	0.26	2.65	0.34	1
S3	616	2.75	96	8	300	0.27	2.66	0.35	1
WS1	616	2.75	96	3	290	0.26	2.65	0.34	1
WS3	616	2.75	96	8	290	0.27	2.66	0.34	1
T1	411	2.81	64	5	190	0.28	2.40	0.33	30
T2	N/A	N/A	64	5	200	0.28	2.66	0.39	30
R1	706	2.81	96	5	350	0.27	2.40	0.35	10
R2	1036	2.81	128	5	550	0.27	2.39	0.37	10
R3/A4	1394	2.81	160	5	800	0.27	2.39	0.39	10
R4	1779	2.81	192	5	1090	0.28	2.39	0.41	10
R5	2394	2.81	240	5	1560	0.28	2.40	0.43	10
A1	1394	0.057	160	5	840	0.006	2.40	0.41	10
A2	1394	0.562	160	5	850	0.06	2.40	0.41	10
A3	1394	1.684	160	5	830	0.17	2.40	0.40	10
A5	1394	4.493	160	5	770	0.42	2.39	0.38	10
C25	2900	2.343	288	5	2010	0.24	2.49	0.45	10
C31	4544	2.343	448	5	3360	0.24	2.77	0.47	1

Table 4. List of HBT simulation cases.

at 1, 1 and 0.01, respectively, while ν and P_λ are adjusted to control Re_{HBT} and At_{HBT}. The last output column in table 4 provides the ratio between the turbulence length scale $l = u_{rms}^{3/2}/\widetilde{\epsilon} = (2/3)^{3/2}\widetilde{k}^{3/2}/\widetilde{\epsilon}$ and the domain length L for each case. Each simulation case is run over M realizations, each with an independently randomized set of initial conditions.

The first four sets of cases serve to determine the optimal numerical parameters for the remaining cases. The 'K' indicates the numerical resolution metric $\kappa_{max}\eta^*$, which is varied between 1.5 and 4. The 'S' refers to the number of subiterations used in the time integration scheme described in § 4.1, set to either 3, 5 or 8. The 'W' refers to the cases using the WENO5 Eulerian scalar scheme (Xu & Shu 2005), as opposed to the semi-Lagrangian BCH (Verma *et al.* 2014) used in every other case. The results of these studies are presented in Appendix A. In short, they suggest that a $\kappa_{max}\eta^* \geqslant 2.4$ with the BCH scheme is sufficient to reduce the numerical scalar diffusion to an acceptable level (namely, 4 % of the total diffusion), and that five subiterations are sufficient to reduce the mass conservation error in the scalar transport equation to negligible levels.

The T1 and T2 cases are sets of 30 realizations with independently randomized initial conditions. These are analysed in §§ 5.2 and 5.3 to study properties of time-series data

https://doi.org/10.1017/jfm.2026.11779 Published online by Cambridge University Press

in HBT. Here T1 uses the fluctuation reduction method described in § 3.2. The reduction method is omitted in T2, with $g = 0.28$, $1/(\alpha\lambda_o) = -2.20$ and $\nu = 0.00077$.

The next set of simulations, labelled 'R', examines the dependence of the flow statistics on the Reynolds number. The number of cells N in each direction is varied from 96 to 240, while ν is adjusted to keep $\kappa_{max}\eta^*$ constant at 2.4. Likewise, the cases labelled 'A' examine the dependence of statistics on the Atwood number. Relating At_{eff} to At via the results of figure 1(*b*), these simulations correspond to SRT/TRT cases with $At \approx 0.01, 0.13, 0.36, 0.55, 0.78$. Ten independent realizations are performed for each case to quantify statistical uncertainties. The results are discussed in § 5.4.

Finally, two cases, C25 and C31, are performed at larger Reynolds numbers to match the conditions of the TRT simulation from Cabot & Cook (2006). For C25, Re_t^* and At_{eff}^* are chosen to match the midplane data of Cabot & Cook (2006) at $t = 25\tau_\Delta$, and C31 at $t = 31\tau_\Delta$, where

$$\tau_\Delta = \sqrt{\frac{32\Delta x}{gAt}} \tag{4.1}$$

and Δx is the grid spacing. At $t = 25\tau_\Delta$, $Re_t|_{x_1=0} = 1930$ and $At_{eff}|_{x_1=0} = 0.23$; at $t = 31\tau_\Delta$, $Re_t|_{x_1=0} = 3690$ and $At_{eff}|_{x_1=0} = 0.23$. The corresponding statistics are compared in § 6.

5. Framework verification

The HBT framework was developed to generate statistically homogeneous data representing SRT, and by extension TRT, in the vicinity of the midplane. In § 5.1, a qualitative comparison is made between a TRT case and an HBT case. In § 5.2, we assess HBT time-series data for qualitative similarity to SRT and statistical stationarity. In § 5.3 the ability of HBT time-averages to converge to ensemble averages is verified and quantified. Section 5.4 leverages HBT results to formulate a regression and estimate the values of non-dimensional flow statistics *a priori*.

5.1. *Qualitative comparison*

Figure 7 shows density fields for both the TRT DNS case of Goh & Blanquart (2025) and the R4 case of HBT. The TRT clearly shows the heavy and light fluid ($\rho_H = 3\rho_L$) reservoirs at the top and bottom of the domain, with a highly turbulent region of high density variance at the centre. The HBT field, despite lacking the reservoirs, maintains a similar degree of density variance via the mean gradient term in (2.48), with the density fluctuating more than 40 % above and below the mean value. The black box in the HBT field has width equal to the turbulence length scale l. As this length scale is of the order of the correlation length scale, the HBT domain can be viewed as a grid of independent realizations of the homogeneous flow, each the size of a cube of width l.

The insets at the centre of figure 7 illustrate the modelling capability of HBT. A small region near the midplane of the Goh & Blanquart (2025) TRT DNS is seen to resemble the l-sized region of the HBT. Thus, the turbulence of HBT models the small scales of TRT near the midplane, at least up to the length scale where the assumptions of § 2.4 remain valid. While this comparison is qualitative, a quantitative comparison of cases, where the non-dimensional parameters of the TRT and HBT are more precisely matched, is made in § 6.

https://doi.org/10.1017/jfm.2026.11779 Published online by Cambridge University Press

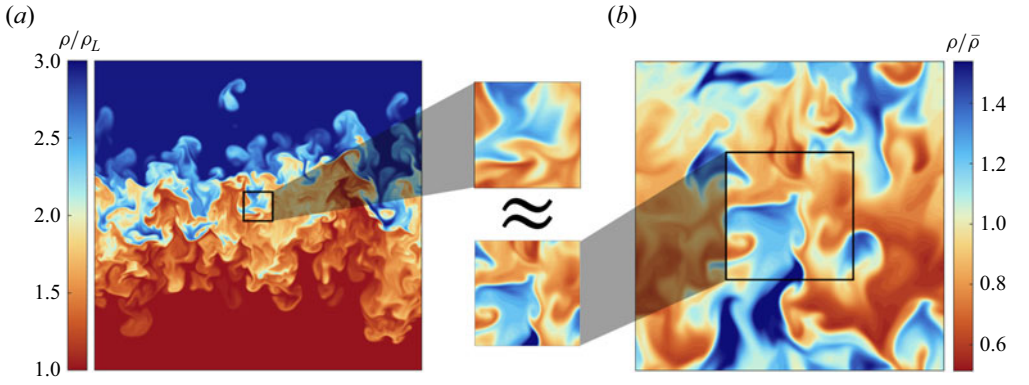


Figure 7. Qualitative comparison of TRT and HBT. Panel (*a*) shows the density field of the $At = 0.5$ TRT DNS conducted by Goh & Blanquart (2025), where the bulk Reynolds number (definition in Cabot & Cook 2006) is ≈ 6400. Panel (*b*) shows the density field of the R4 HBT case. Each field is normalized by the dimensional input which sets the density scale (ρ_L for TRT, $\overline{\rho}$ for HBT). The square region of the HBT field highlighted by the inset has size equal to the turbulence length scale l.

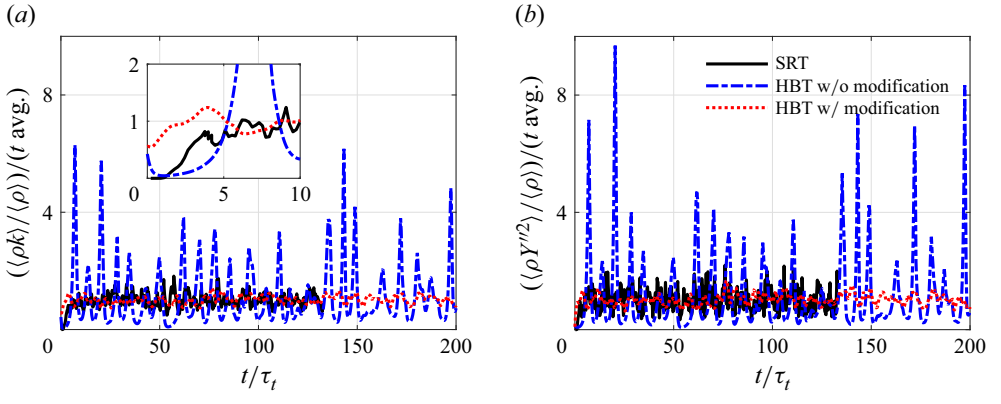


Figure 8. Time series data for the density-weighted volume averages of (*a*) the turbulent kinetic energy and (*b*) the scalar variance for single T1 and T2 HBT realizations, as well as the G3 SRT case of Goh & Blanquart (2025). Values are normalized by the time-average.

5.2. *Time-series data*

The HBT framework is intended to model the results of SRT in the vicinity of the midplane. For the model to be successful, time-series data from HBT must both qualitatively resemble SRT time-series data at the midplane and, like SRT, be stationary in time. These properties are tested for HBT results both with and without the source term modification described in § 3.2.

Figure 8(*a*,*b*) shows the density-weighted volume averages of kinetic energy and scalar variance over time (single realizations from the T1 and T2 cases of table 4). These are shown alongside midplane data of the corresponding G3 SRT case of Goh & Blanquart (2025). Qualitatively, the simulations appear stationary in time after a short transient evolution, visible in the inset of figure 8(*a*). Judging from the location of the second crossing of the time-average, the transient lasts until approximately $t = 8\tau_t$ for the unmodified HBT, $t = 5\tau_t$ for the modified and $t = 7\tau_t$ for SRT. All SRT and HBT time-averages reported in this study are calculated using only data after these times.

https://doi.org/10.1017/jfm.2026.11779 Published online by Cambridge University Press

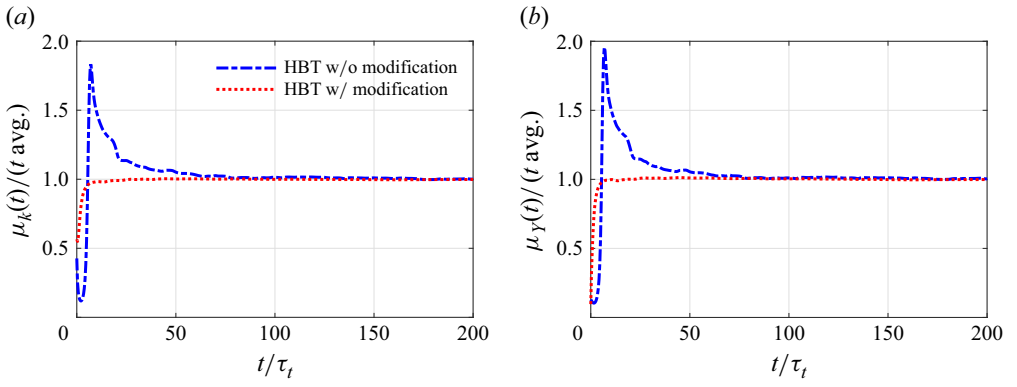


Figure 9. Average across realizations of the cumulative time-averages of the density-weighted volume averages of (*a*) the turbulent kinetic energy and (*b*) the scalar variance.

Both the kinetic energy and scalar variance of the unmodified HBT have strong intermittent fluctuations as high as eight times the time-average, with relative standard deviations of approximately 1.3 for kinetic energy and 1.8 for scalar variance. With the modification, the intermittency is removed and the relative standard deviations are ≈ 0.13 and ≈ 0.17. Although the SRT fluctuations have larger relative standard deviations (≈ 0.25 and ≈ 0.36) than the modified HBT, they are not intermittent and clearly bear a stronger resemblance to the modified HBT than the unmodified. The modification not only succeeds in reducing the magnitude of the temporal fluctuations, but also improves their fidelity by bringing them further in line with SRT data.

Figure 9(*a*,*b*) shows the cumulative time-averages for the density-weighted volume averages of kinetic energy and scalar variance, averaged across all realizations in cases T1 and T2. These are defined as

$$\mu_k(t) = \frac{1}{M}\left(\sum_{m=1}^{M}\frac{1}{t}\int_0^t \frac{\langle \rho k\rangle_m}{\langle\rho\rangle_m}\mathrm{d}t'\right), \quad \mu_Y(t) = \frac{1}{M}\left(\sum_{m=1}^{M}\frac{1}{t}\int_0^t \frac{\langle \rho Y''^2\rangle_m}{\langle\rho\rangle_m}\mathrm{d}t'\right) \tag{5.1}$$

where $\langle\cdot\rangle_m$ refers to data associated with realization m, and M is the total number of realizations. The cumulative averages converge to values that are constant in time, showing that the flow arrives at a statistically stationary state.

The correlation time scale, which quantifies the 'memory' of the flow, is calculated as

$$\tau_{corr} = \int_0^\infty R_F(\tau)\mathrm{d}\tau \tag{5.2}$$

where $R_F(\tau)$ is the autocorrelation function of time series F:

$$R_F(\tau) = \frac{\overline{F(t+\tau)F(t)} - \overline{F(t+\tau)}\,\overline{F(t)}}{\overline{F^2} - \overline{F}^2}. \tag{5.3}$$

The correlation functions for the kinetic energy and scalar variance are shown in figure 10(*a*,*b*). The unmodified function overshoots zero then oscillates for a time, while the modified relaxes to zero smoothly. To estimate the correlation time scale of (5.2), the integral is taken up to the first zero-crossing in both cases, and their values are given as annotations. In both cases, $\tau_{corr} \approx \tau_t$. While the time correlation values are similar, the tendency of the unmodified correlation to oscillate suggests that some pointwise autocorrelations persist over long times. This has implications for the length of the

https://doi.org/10.1017/jfm.2026.11779 Published online by Cambridge University Press

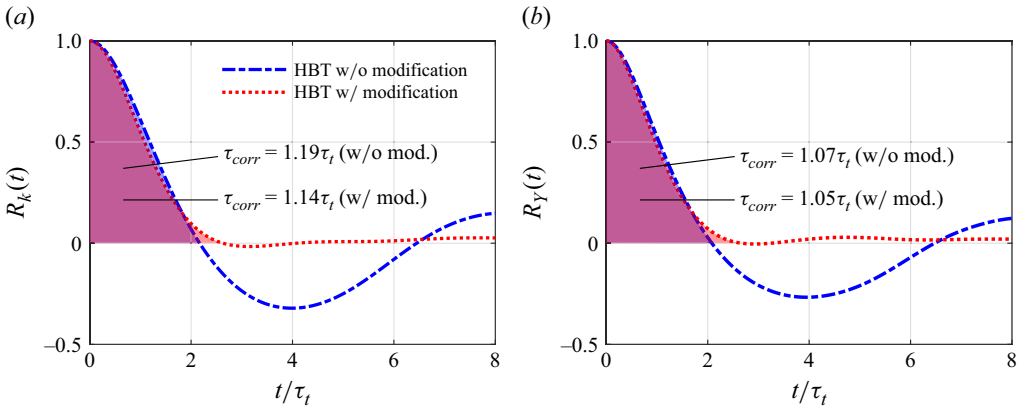


Figure 10. Autocorrelation functions for the density-weighted volume averages of (*a*) the turbulent kinetic energy and (*b*) the scalar variance. Averages have been taken across all realizations of each case. The shaded areas represent the integral up to the first zero-crossing, an estimate of the correlation time scale τ_{corr}.

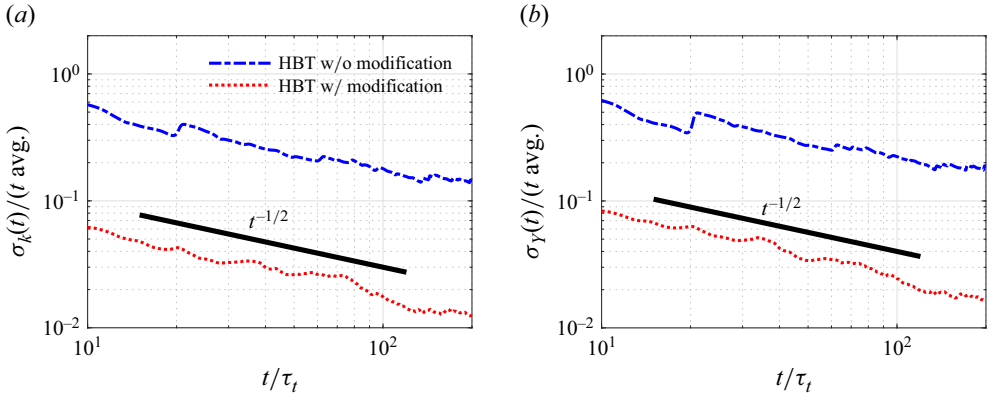


Figure 11. Sample standard deviation across realizations of the cumulative time-averages of the density-weighted volume averages of (*a*) the turbulent kinetic energy and (*b*) the scalar variance.

unmodified transient period, which may extend, through long-term correlations with the initial conditions, even further than can be inferred from the inset of figure 8(*a*).

5.3. *Time-averaging*

A key advantage of HBT is its ability to produce converged statistics quickly by averaging over all spatial directions and time. As larger simulation times are reached, these time-averages should approach ensemble averages that are independent of the initial conditions.

To verify this and measure the rate of convergence, figure 11(*a*,*b*) shows the sample standard deviation across realizations of cumulative time-averages of kinetic energy and density-weighted scalar variance. For the kinetic energy, this is

$$\sigma_k(t) = \left\{ \frac{1}{M-1} \sum_{m=1}^{M} \left[\left(\frac{1}{t} \int_0^t \frac{\langle \rho k \rangle_m}{\langle \rho \rangle_m} \mathrm{d}t' - \frac{1}{M} \sum_{n=1}^{M} \frac{1}{t} \int_0^t \frac{\langle \rho k \rangle_n}{\langle \rho \rangle_n} \mathrm{d}t' \right)^2 \right] \right\}^{1/2} \tag{5.4}$$

https://doi.org/10.1017/jfm.2026.11779 Published online by Cambridge University Press

and for the density-weighted scalar variance

$$\sigma_Y(t) = \left\{ \frac{1}{M-1} \sum_{m=1}^{M} \left[\left(\frac{1}{t} \int_0^t \frac{\langle \rho Y''^2 \rangle_m}{\langle \rho \rangle_m} \mathrm{d}t' - \frac{1}{M} \sum_{n=1}^{M} \frac{1}{t} \int_0^t \frac{\langle \rho Y''^2 \rangle_n}{\langle \rho \rangle_n} \mathrm{d}t' \right)^2 \right] \right\}^{1/2}. \tag{5.5}$$

The standard deviations of both cases decay with time roughly as $t^{-1/2}$. This is the asymptotic relationship between the standard deviation of the mean of independent and identically distributed samples, and the number of samples in the mean. This implies that each cumulative time-average can be seen as an independent sample mean from the same statistical population. Thus, the initial conditions, independently randomized for each realization, do not affect the final flow statistics.

Between the unmodified and modified cases in figure 11(*a*,*b*), the modified case has a lower standard deviation at all times by approximately an order of magnitude. This is apparently due to the mitigation of temporal fluctuations, also by an order of magnitude, described in § 5.2 and illustrated in figure 8(*a*,*b*). While the unmodified HBT retains a large deviation (greater than 10 %) even after $200\tau_t$ of simulation, the modified HBT reaches a deviation of 3 % after only $40\tau_t$. For this reason, along with the increased resemblance to SRT in figure 8(*a*,*b*) and the absence of long-term correlations in figure 10(*a*,*b*), the modified HBT is proposed as the 'true' HBT formulation and is used in all other cases. Simulations are run to $t = 40\tau_t$ to measure time-average statistics throughout the study, unless stated otherwise.

5.4. *Statistical scalings*

As discussed in § 3.3, to produce an HBT flow analogous to a particular TRT, the non-dimensional statistics Re_t^* and At_{eff}^* of the HBT must be adjusted with reference to the values of $Re_t|_{x_1=0}$ and $At_{eff}|_{x_1=0}$ in the TRT. However, producing desired values for these parameters in HBT is not possible without *a priori* knowledge of the relationship between the HBT inputs and the Re_t^* and At_{eff}^* outputs.

Parts of this relationship can be immediately deduced through known scalings of flow statistics with input parameters. For example, the energy injection rate P_g scales with the viscous dissipation $\widetilde{\epsilon}$ in a stationary state. The length scale $l = u_{rms}^{3/2}/\widetilde{\epsilon} = (2/3)^{3/2}\widetilde{k}^{3/2}/\widetilde{\epsilon}$ has been measured as $\approx 0.2L$ in HIT (Rosales & Meneveau 2005); it is reasonable to assume a similar scaling applies in HBT. The scalar variance is assumed to be proportional to the product of the injection rate P_λ and the only time scale obtainable from L and P_g, namely $L^{2/3}/P_g^{1/3}$. Finally, ρ_{rms} scales with the scalar variance and the derivative of the EoS $Y(\rho)$ (this scaling changes when an EOS other than (2.8) is used). Under these assumptions, scalings for the non-dimensional statistics are

$$Re_t^* = C_{Re}\frac{L^{4/3}P_g^{1/3}}{\nu} = C_{Re}Re_{HBT}, \qquad At_{eff}^* = C_{At}\frac{\alpha\overline{\rho}P_\lambda^{1/2}L^{1/3}}{P_g^{1/6}} = C_{At}At_{HBT} \tag{5.6}$$

where C_{Re} and C_{At} represent coefficients of proportionality and Re_{HBT} and At_{HBT} are the non-dimensional input parameters defined in § 3.3. Although the scalings should account for most of the variation, the coefficients may still exhibit dependence on Re_{HBT} and At_{HBT}. To measure this dependence, the coefficients of cases T1 and R1–5 are extracted and plotted against Re_{HBT} in figure 12(*a*,*b*), and cases A1–5 against At_{HBT} in figure 13(*a*,*b*). Error bars represent a 96 % confidence interval for each data point, assuming a Gaussian distribution for each set of realizations.

https://doi.org/10.1017/jfm.2026.11779 Published online by Cambridge University Press

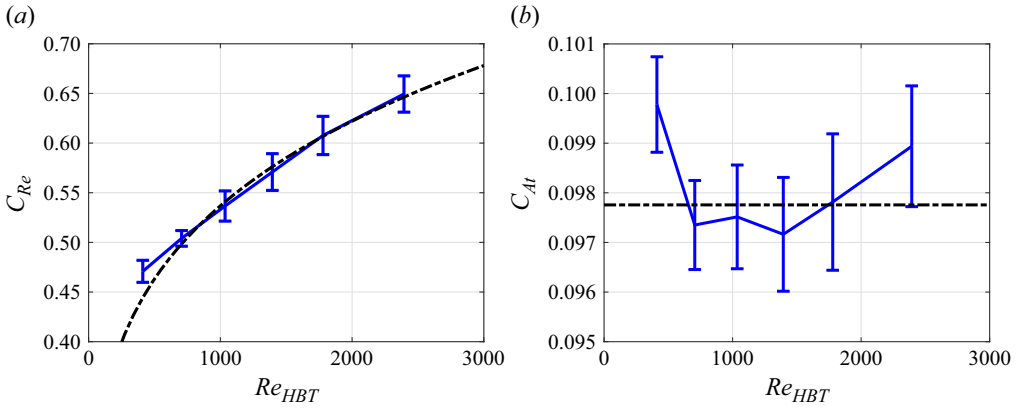


Figure 12. Proportionality coefficients for (*a*) C_{Re} and (*b*) C_{At} versus Re_{HBT} for cases T1 and R1-5 (blue solid). The error bars indicate the standard deviation across realizations, multiplied by 2 and divided by the square root of the number of realizations. A power law fit based on cases R1–5 is shown for C_{Re}, and the average value of cases R1–5 is shown for C_{At} (black dash–dotted).

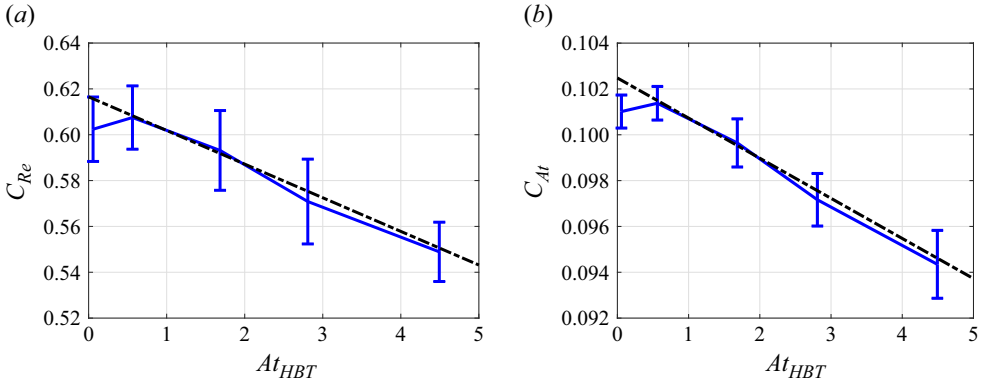


Figure 13. Proportionality coefficients for (*a*) C_{Re} and (*b*) C_{At} versus At_{HBT} for cases A1–5 (blue solid). The error bars indicate the standard deviation across realizations, multiplied by 2 and divided by the square root of the number of realizations. Linear regressions from cases A2–5 for C_{Re} and from cases A1–5 for C_{At} are also shown (black dash–dotted).

Here C_{At} shows very little sensitivity to Re_{HBT}, varying by only 2 % from $Re_{HBT} = 400$ to $Re_{HBT} = 2400$. After a drop from $Re_{HBT} = 400$ to $Re_{HBT} = 700$ (possibly a low Reynolds number effect), a slight upwards trend is seen up to $Re_{HBT} = 2400$, barely strong enough to be statistically meaningful. More sensitivity is seen in the relationship between C_{At} and At_{HBT}, which shows a stable downward trend from $At_{HBT} = 0.6$ to $At_{HBT} = 4.5$ as C_{At} descends approximately 7 %. Meanwhile, C_{Re} shows a relatively strong sensitivity to Re_{HBT}, rising by more than 40 % from $Re_{HBT} = 400$ to $Re_{HBT} = 2400$. It has a negative trend with At_{HBT}, descending approximately 10 % from $At_{HBT} = 0.6$ to $At_{HBT} = 4.5$. There is no clear trend in either C_{Re} or C_{At} with At_{HBT} below $At_{HBT} = 0.6$, probably because the variable-density effects are not significant in that range.

To extend the relationships plotted in figures 12(*a*,*b*) and 13(*a*,*b*) to arbitrary values, regressions for C_{Re} and C_{At} are produced. A power law fit is used to relate C_{Re} to Re_{HBT}, shown in figure 12(*a*). Here C_{At} is insensitive enough to Re_{HBT} that, while a slight positive trend is present, a constant value can be assumed without significant error. Therefore, the

https://doi.org/10.1017/jfm.2026.11779 Published online by Cambridge University Press

Coefficient	$C \approx (aAt_{HBT} + b)Re^{c}_{HBT}$		
	$a \times 10^3$	$b \times 10^1$	$c \times 10^1$
C_{Re}	−3.28	1.33	2.13
C_A	−1.82	1.02	0

Table 5. Parameters for scaling coefficient regressions.

regression for C_{At} with respect to Re_{HBT} is just an average value (indicated by a horizontal line in figure 12*b*). Meanwhile, linear fits are used for both regressions in At_{HBT}. These are shown in figure 13(*a*,*b*). In calculating coefficients for the regressions with respect to Re_{HBT}, the data point around $Re_{HBT} = 400$ is ignored to avoid low-Reynolds number effects. The data point around $At_{HBT} = 0.05$ is also ignored to focus on conditions where variable-density effects are significant.

Since R3 and A4 are the same test case, the regressions of C_{Re} with respect to Re_{HBT} and At_{HBT} approximately intersect in Re_{HBT}–At_{HBT}–C_{Re} space. For this coefficient, a fit containing both regressions can be defined as a bivariate function of Re_{HBT} and At_{HBT}, alongside the univariate fit for C_{At}:

$$C_{Re} = (a_R At_{HBT} + b_R)Re^{c}_{HBT}, \tag{5.7}$$

$$C_{At} = a_A At_{HBT} + b_A. \tag{5.8}$$

The parameters a, b and c for each regression are given in table 5.

The regressions can be combined with the scalings of (5.6) to derive formulae for the non-dimensional inputs given the desired non-dimensional outputs:

$$Re_{HBT} = Re_t^{*\frac{1}{c+1}} \left(a_R \frac{-b_A + \sqrt{b_A^2 - 4a_A At^*_{eff}}}{2a_A} + b_R \right)^{-\frac{1}{c+1}}, \tag{5.9}$$

$$At_{HBT} = \frac{-b_A + \sqrt{b_A^2 - 4a_A At^*_{eff}}}{2a_A}. \tag{5.10}$$

To model the midplane of any given TRT, its values of $Re_t|_{x_1=0}$ and $At_{eff}|_{x_1=0}$ can be substituted for Re_t^* and At^*_{eff} in (5.9) and (5.10) to obtain the necessary inputs for HBT.

It is interesting to note that $C_{Re} \propto (l/L)^{4/3}$, so that one consequence of C_{Re} rising with Re_t^* is that the turbulence length scale l increases relative to the domain length L. This is apparent from table 4, where l/L rises from 0.35 to 0.43 over cases R1–5. This is larger than the HIT value of 0.2 (Rosales & Meneveau 2005), so a larger range of length scales can be represented at a given domain size in HBT compared with HIT.

5.5. *Cascade dynamics*

In addition to matching stationary statistics, HBT is expected to reproduce the turbulent dynamics of SRT and TRT across length scales. To compare the cascade dynamics, figure 14(*a*,*b*) shows the 2-D spectral budgets of kinetic energy and scalar variance for both the midplane of the G4 SRT case and the R1 HBT case. Details on how these budgets are calculated are included in Appendix C.

The terms of HBT and SRT nearly collapse at all but the smallest four wavenumbers, demonstrating that the small-scale time dynamics of SRT and TRT turbulence is captured by HBT. The errors in the large scales are limited to the convection, pressure, buoyancy

https://doi.org/10.1017/jfm.2026.11779 Published online by Cambridge University Press

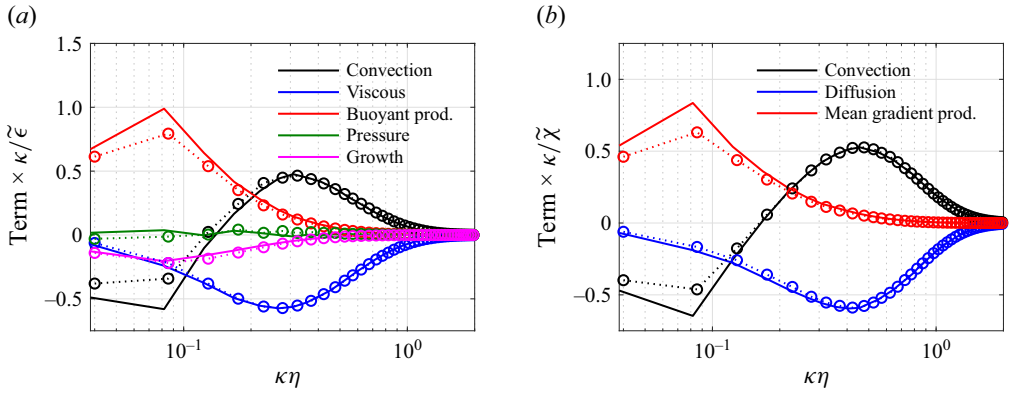


Figure 14. The 2-D planar spectral budgets for (*a*) kinetic energy and (*b*) scalar variance for both the midplane of the G4 SRT case (solid lines) and the R1 HBT case (dotted lines). Terms are multiplied by κ for visibility. To avoid statistical fluctuations, the convection is computed indirectly by subtracting the remaining terms from zero.

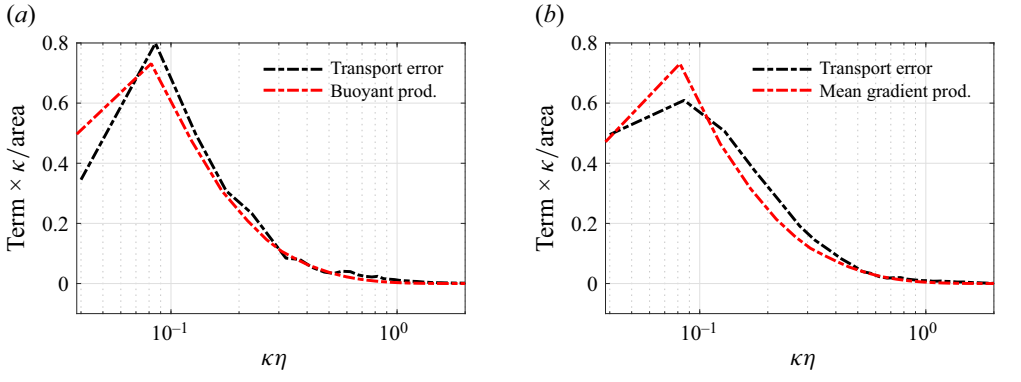


Figure 15. Errors in the (*a*) energy transport (pressure + convection) and (*b*) scalar variance transport (convection) spectral budget terms of figure 14(*a*,*b*), plotted alongside the SRT buoyant and mean gradient production terms, respectively. Terms are normalized so that the apparent areas under their curves are equal.

and mean gradient production terms. This is expected, as the convection and pressure terms in SRT include the transport terms and other terms neglected in HBT, which were modelled by a reduction in the buoyant and mean gradient production terms, as discussed in § 3.1.

As a verification of this modelling approach, figure 15(*a*,*b*) shows the difference in the sum of pressure and convection between HBT and SRT in the kinetic energy and scalar variance spectral budgets, alongside the corresponding production terms. The resemblance in the shape of the kinetic energy transport error to the buoyant production, and scalar variance transport error to the mean gradient production, indicates that the former can be reasonably modelled by a constant multiple of the latter.

6. Comparison with TRT simulations

Using (5.9) and (5.10) as a starting point, followed by manual tuning, the parameters of cases C25 and C31 were selected to be representative of the midplanes of the Cabot & Cook (2006) TRT at $t = 25\tau_\Delta$ and $t = 31\tau_\Delta$, respectively. Data from the corresponding

https://doi.org/10.1017/jfm.2026.11779 Published online by Cambridge University Press

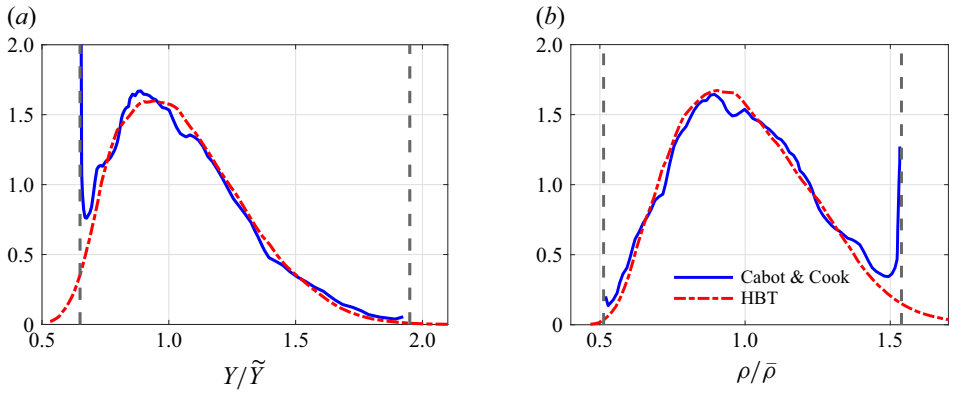


Figure 16. Probability density functions for normalized (*a*) scalar and (*b*) density from case C25 and the midplane of the Cabot & Cook (2006) TRT at $t = 25\tau_\Delta$. They are calculated over the two horizontal directions for TRT and all spatial directions and time for HBT. Cabot & Cook (2006) values are derived from the data of digitized plots from Livescu *et al.* (2010). Dashed vertical lines indicate the properties of pure heavy/light fluid in TRT.

TRT and HBT cases are now compared to validate HBT's fidelity. Three categories of flow metrics are discussed: the probability density function (PDF) of the density, the anisotropy of the velocity field and its derivatives, and the velocity/density spectra.

6.1. *Probability density functions*

Figure 16(*a*,*b*) shows the scalar and density PDFs of Cabot & Cook (2006) overlain with those of case C25. The TRT PDFs are taken at the midplane over only the two horizontal directions at an instant in time ($t = 25\tau_\Delta$), whereas the HBT PDFs are taken over all spatial directions and time. The scalar has been normalized by $\widetilde{Y}$, and the density by $\overline{\rho}$.

For both density and scalar, the TRT and HBT PDFs share the same qualitative shape: a skewed bell curve. Differences between the TRT and HBT distributions are small enough over most of the distribution to be attributed to statistical fluctuations. Noteworthy differences appear only near the edges of the distributions; while HBT smoothly decays to zero at both ends, the TRT distributions spike upward then stop at distinct limits. These two limits correspond to the properties of pure heavy/light fluids. The violation of these bounds in HBT arises from the introduction of a source term to the scalar transport (2.48). Since the discrepancies are limited to the fringes of the distribution, which account for only a small fraction of the total fluid mass, HBT's overall fidelity seems to have not been harmed by the loss of imposed scalar bounds. The implications of the lack of imposed bounds on the density and scalar extrema in HBT are addressed in Appendix B.

The HBT profile is also noticeably smoother than the TRT, having converged further towards a true ensemble average. This is a consequence of HBT's PDF having been taken across time and three spatial directions, as opposed to Cabot & Cook (2006)'s evaluation at a single plane and at a single time step. This demonstrates the advantage of a statistically stationary framework like HBT.

6.2. *Velocity anisotropy*

Figure 17(*a*) shows the ratio of variances of the vertical and horizontal components of velocity, measured across horizontal planes at varying x_1 locations in the Cabot & Cook (2006) TRT and measured over space and time for case C25 of HBT. The variances of horizontal components $\overline{u_2'^2}$ and $\overline{u_3'^2}$ are averaged together, since they are statistically

https://doi.org/10.1017/jfm.2026.11779 Published online by Cambridge University Press

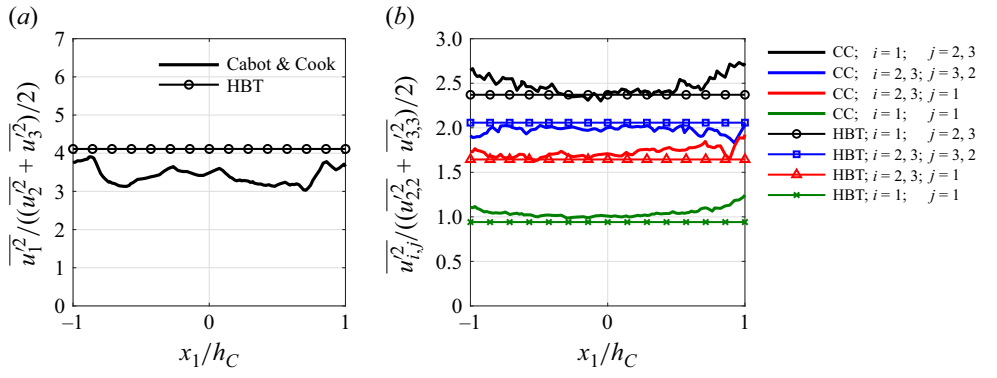


Figure 17. Variances of (*a*) the vertical velocity normalized by the variance of the horizontal velocity and (*b*) the velocity gradient tensor normalized by the variance of the longitudinal derivative of horizontal velocity. Data is shown for the Cabot & Cook (2006) TRT at $t = 25\tau_\Delta$ and case C25. Variances are calculated over horizontal planes at varying x_1 values for Cabot & Cook (2006) and across space and time for case C25. Where i or j takes more than one value, quantity is the average of the components with the corresponding indices. Cabot & Cook (2006) values are derived from plots of Cabot & Zhou (2013). In the legend CC stands for Cabot & Cook (2006).

equivalent. The x_1 coordinate is normalized by h_C, the layer height definition used by Cabot & Cook (2006):

$$h_C = \frac{2}{\rho_L + \rho_H} \int_{=\infty}^{\infty} \min(\langle \rho - \rho_L \rangle_{2\text{-D}}, \langle \rho_H - \rho \rangle_{2\text{-D}}) \mathrm{d}x_1. \tag{6.1}$$

For both HBT and TRT, the ratio is well above 1 (the value expected in an isotropic flow). This is because kinetic energy is initially deposited within the vertical component of velocity by buoyancy, which is then distributed to the other components by pressure and convective transport. This induces a buildup of energy in the vertical component, such that in a self-similar state in TRT, or a stationary state in HBT, the velocity fluctuations in the vertical direction are several times more energetic than those in the horizontal directions. It is interesting to note that the ratio in TRT is uniform (within statistical uncertainty) across a large region of the mixing layer. The HBT value overpredicts the ratio by approximately 10 % to 20 %.

Figure 17(*b*) shows the variances of each component of the velocity gradient tensor, $\overline{(\partial u_i'/\partial x_j)^2} = \overline{u_{i,j}'^2}$, normalized by the variance of the horizontal longitudinal velocity derivative, $\overline{u_{2,2}'^2}$. Once again, any components that are statistically equivalent due to horizontal isotropy are averaged together.

In a fully homogeneous isotropic flow with uniformly zero divergence of velocity, the normalized variances would be 1 for all longitudinal derivatives and 2 for all transverse derivatives. Although the divergence is not exactly zero here, $\overline{u_{2,3}'^2}$ is within 1 % of the value guaranteed by zero divergence, namely $3\overline{u_{2,2}'^2} - \overline{u_{1,1}'^2}$, for both HBT and TRT. Since the presence of divergence has a negligible influence on the gradient component variances, their deviation from the isotropic values can be attributed exclusively to anisotropy in the velocity field.

The HBT results successfully predict all TRT normalized variances within a few per cent. For both TRT and HBT, the variance of the horizontal derivative of vertical velocity, $\overline{u_{1,2}'^2}$, is greater than the isotropic value of $2\overline{u_{2,2}'^2}$ by approximately 17 %, while the vertical

https://doi.org/10.1017/jfm.2026.11779 Published online by Cambridge University Press

derivative of horizontal velocity, $\overline{u'^2_{2,1}}$, is lower by approximately 17 %. As observed by Cabot & Zhou (2013), this implies that the anisotropy manifests both as an increased vertical velocity intensity (as seen in figure 17*a*) and increased vertical Taylor length scales,

$$\lambda_{i1} = \left(\frac{\overline{u_i'^2}}{\overline{u_{i,1}'^2}} \right)^{1/2}, \tag{6.2}$$

relative to the corresponding length scales associated with horizontal derivatives. For the longitudinal vertical gradient variance $\overline{u'^2_{1,1}}$, the velocity anisotropy compensates the length scale anisotropy, so that it is nearly identical to its horizontal counterpart $\overline{u'^2_{2,2}}$. Like the velocity variances, the relative magnitudes of the gradient component variances are nearly constant across the TRT layer. They deviate no more than 5 % from the midplane value at a distance of $h_C/2$.

The variances of the velocity components and the velocity gradient components are representative of the large and small length scales of the velocity field, respectively. The fact that HBT is able to capture the anisotropy of the velocity gradient (within a few per cent), as well as the velocity itself (within 17 %), indicates that HBT quantitatively models the small scales of TRT while retaining a qualitative resemblance at the larger scales. Most of the error associated with HBT, attributable to violation of the assumptions discussed in § 2.4, seems to be isolated from the finer turbulence structure. Notably, the near-uniformity of the TRT ratios with x_1 suggests a degree of universality in HBT's representation of buoyant turbulence, beyond its intended local applicability to the TRT midplane.

6.3. *Spectra*

Because a TRT is isotropic and homogeneous in the two horizontal directions, 2-D energy spectra can be obtained for any two quantities at any x_1 location. The 2-D Fourier transform of a function defined on a horizontal plane is indicated by

$$G(k_2, k_3) = \mathscr{F}^{2\text{-D}}\{g(x_2, x_3)\} \tag{6.3}$$

where k_i are the components of the wavevector. The energy spectrum is obtained by multiplying the transform by the conjugate of the Fourier transform of a second quantity, taking the real part, then integrating over annuli of wavenumbers,

$$E^{2\text{-D}}_{gh}(\kappa) = \int_0^{2\pi} \mathrm{Re}[G(\kappa, \theta) H^*(\kappa, \theta)] \kappa \, \mathrm{d}\theta, \tag{6.4}$$

where a transformation to polar coordinates in horizontal wavenumber space is applied,

$$\kappa^2 = k_2^2 + k_3^2, \quad k_2 = \kappa \cos(\theta), \quad k_3 = \kappa \sin(\theta). \tag{6.5}$$

The energy spectrum integrates to the planar covariance of the two variables,

$$\int_0^\infty E^{2\text{-D}}_{gh}(\kappa) \mathrm{d}\kappa = \langle gh \rangle_{2\text{-D}} - \langle g \rangle_{2\text{-D}} \langle h \rangle_{2\text{-D}}. \tag{6.6}$$

As the number of samples increase, either by taking the spectrum over a larger plane or averaging over time or x_1 in a stationary homogeneous flow, this integral approaches the ensemble covariance, $\overline{g'h'}$.

Although g and h are treated as continuous variables in the above equations, in practice measurements of the spectrum are taken on a discrete numerical grid. As such, the discrete

https://doi.org/10.1017/jfm.2026.11779 Published online by Cambridge University Press

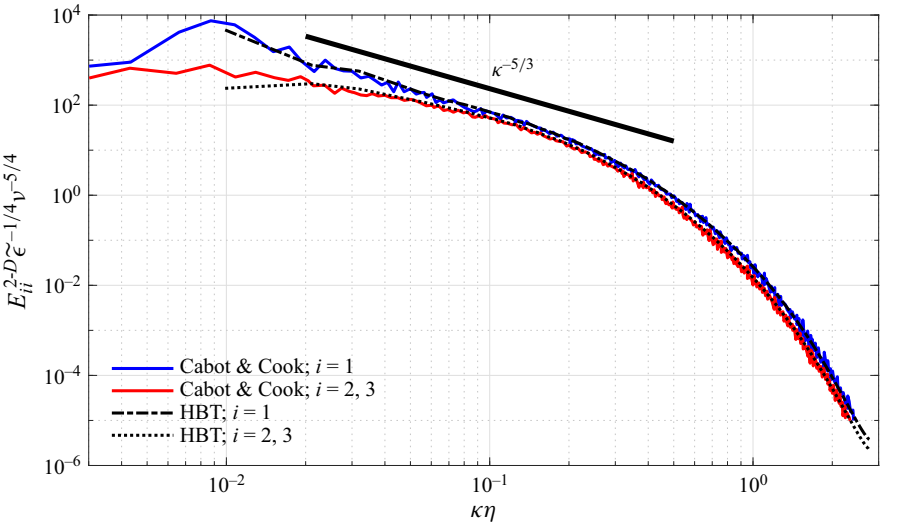


Figure 18. The 2-D planar velocity spectra for the midplane of the Cabot & Cook (2006) TRT at $t = 31\tau_\Delta$ and case C31, normalized by $\widetilde{\epsilon}$ and ν. The C31 spectra are averaged over x_1 and time. Where i takes more than one value, the quantity is the average of the components with the corresponding indices. Cabot & Cook (2006) data are derived from plots of Chung & Pullin (2010), where y-axis values had been cut off below 10^{-5}.

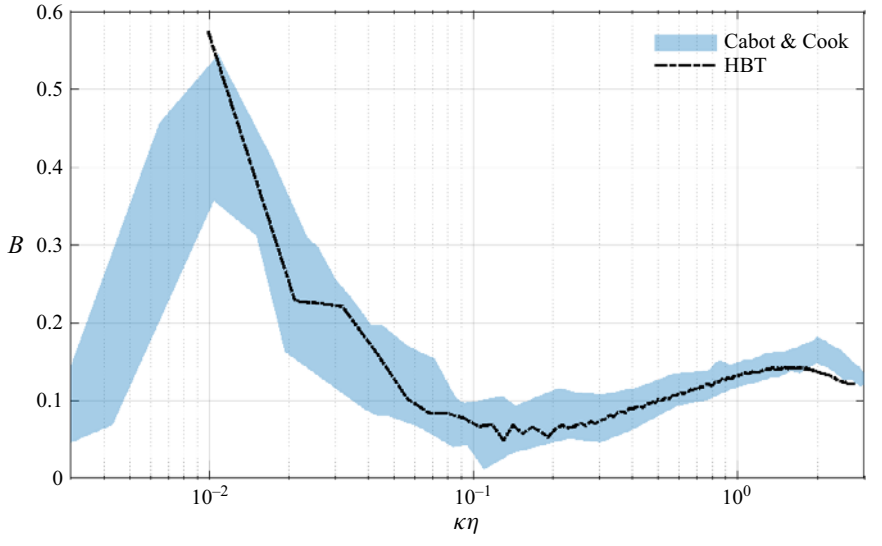


Figure 19. Anisotropy spectra for the midplane of the Cabot & Cook (2006) TRT at $t = 31\tau_\Delta$ and case C31. Cabot & Cook (2006) data are derived from a plot of Chung & Pullin (2010), where x-axis values had been cut off above $\kappa\eta = 3$. The shading represents the approximate range of fluctuations. The C31 data are calculated from the spectra of figure 18, having already been averaged over x_1 and time.

Fourier transform is used and the integral in (6.4) is replaced by averages of grid points over $N/2$ finite annulus-shaped bins associated with discrete values of κ, where N is the number of grid points in a horizontal direction.

The 2-D spectra are presented in figures 18–22 for both the HBT case C31 and the Cabot & Cook (2006) TRT midplane at $t = 31\tau_\Delta$. The wavenumber κ is normalized by

https://doi.org/10.1017/jfm.2026.11779 Published online by Cambridge University Press

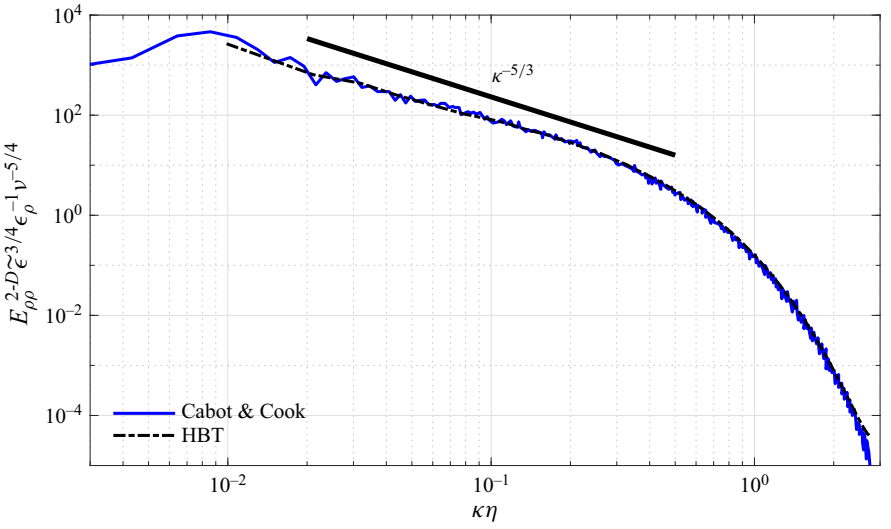


Figure 20. The 2-D planar density spectra for the midplane of the Cabot & Cook (2006) TRT at $t = 31\tau_\Delta$ and case C31, normalized by $\widetilde{\epsilon}$, ϵ_ρ and ν. The C31 spectra are averaged over x_1 and time. Cabot & Cook (2006) data are derived from plots of Chung & Pullin (2010), where y-axis values had been cut off below 10^{-5}.

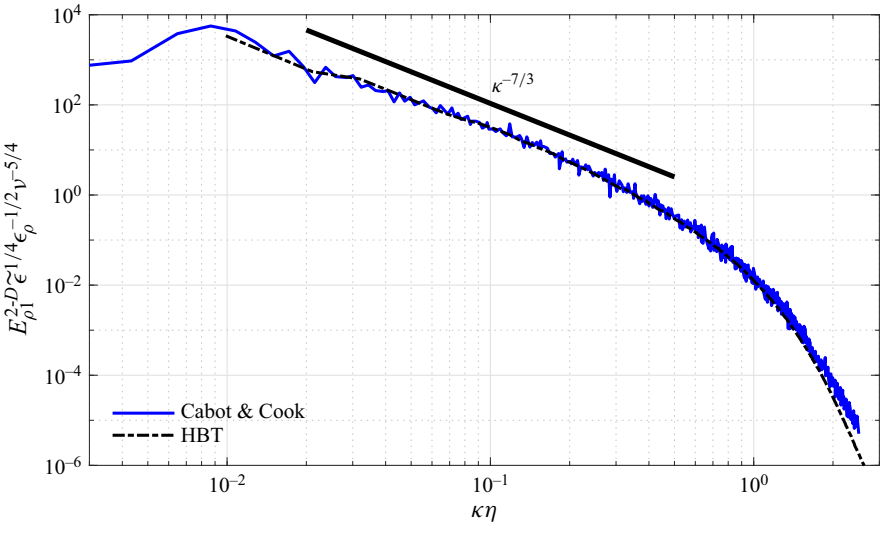


Figure 21. The 2-D planar density–vertical velocity cospectra for the midplane of the Cabot & Cook (2006) TRT at $t = 31\tau_\Delta$ and case C31, normalized by $\widetilde{\epsilon}$, ϵ_ρ and ν. The C31 spectra are averaged over x_1 and time. Cabot & Cook (2006) data are derived from plots of Chung & Pullin (2010), where y-axis values had been cut off below 10^{-5}.

the Kolmogorov length scale. The spectra are normalized by the viscous dissipation $\widetilde{\epsilon}$, the kinematic viscosity ν and the density fluctuation dissipation rate ϵ_ρ, defined by Chung & Pullin (2010) as

$$\epsilon_\rho = D\overline{\left(\frac{\partial \rho}{\partial x_j}\right)^2}, \tag{6.7}$$

https://doi.org/10.1017/jfm.2026.11779 Published online by Cambridge University Press

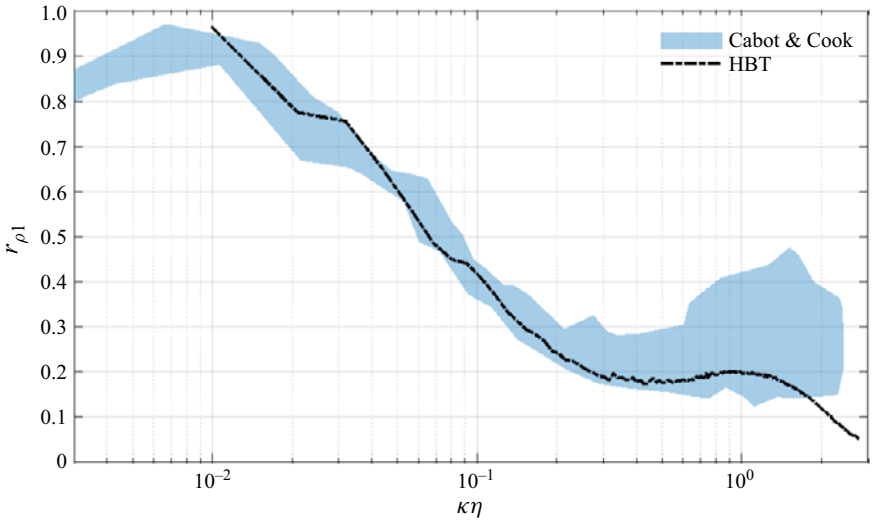


Figure 22. Density–vertical velocity spectral coherence for the midplane of the Cabot & Cook (2006) TRT at $t = 31\tau_\Delta$ and case C31. Cabot & Cook (2006) data are derived from the $E^{2\text{-D}}_{\rho 1}$, $E^{2\text{-D}}_{\rho\rho}$ and $E^{2\text{-D}}_{11}$ plots of Chung & Pullin (2010), where the shading represents the approximate range of fluctuations. The C31 data are calculated from the $E^{2\text{-D}}_{\rho 1}$, $E^{2\text{-D}}_{\rho\rho}$ and $E^{2\text{-D}}_{11}$ spectra of figures 18, 20 and 21, having already been averaged over x_1 and time.

with the appropriate exponents to achieve non-dimensionalization. While the TRT spectra are taken over a single plane, the HBT spectra are averaged across x_1 and six time snapshots. Energy spectra for velocity components u_i and u_j are represented by $E^{2\text{-D}}_{ij}$ throughout the following discussion.

The density–vertical velocity cospectrum is given in figure 21. This spectrum integrates to the density–vertical velocity covariance $\overline{\rho' u_1'}$ and represents the contribution of each wavelength to the buoyant production of turbulent kinetic energy (term VI in (2.40)). Once again, the TRT and HBT data collapse within statistical uncertainty for nearly all wavenumbers, though they diverge slightly in the viscous range beyond $\kappa\eta = 1$. Both appear to exhibit the $\kappa^{-7/3}$ inertial subrange scaling predicted by Lumley (1967) for passive scalar transport in the presence of a mean scalar gradient.

Spectra for the vertical and horizontal velocity are shown in figure 18. These represent contributions to the vertical and horizontal components of the Reynolds-averaged turbulent kinetic energy ($\overline{u_i'^2}$) at different length scales. The horizontal spectrum is averaged from the spectra of u_2 and u_3. The TRT spectra extend over a larger range of length scales than the HBT spectra because HBT uses a smaller computational grid; recall that HBT is intended to model only the small length scales of TRT.

After normalization, the TRT and HBT spectra collapse for nearly all wavenumbers. For $\kappa\eta > 0.1$ the collapse is almost perfect. For $0.02 < \kappa\eta < 0.1$, the HBT spectra lie within the statistical fluctuations of the TRT spectra. The only significant errors appear at the lowest HBT wavenumber, around $\kappa\eta = 0.01$. This represents an improvement on Chung & Pullin (2010)'s stationary buoyancy framework, which overestimated the energy spectra for large wavenumbers. In that study, the authors attributed the discrepancy to the imbalance between the production and dissipation in the TRT, which was not represented in the 'equilibrium' turbulence of their framework. Since the temporal evolution of the TRT has been taken into account by the framework of Goh & Blanquart (2025), which forms the basis for HBT, the discrepancy has been corrected here. For both cases, the

https://doi.org/10.1017/jfm.2026.11779 Published online by Cambridge University Press

standard $\kappa^{-5/3}$ scaling of the inertial subrange (Pope 2001) (indicated by a fiducial in figure 18) is followed closely by the slope of the vertical velocity spectrum. This agrees with the findings of Boffetta *et al.* (2009), who observed that RT turbulence reproduces several HIT inertial range scalings. However, as a result of the anisotropy inherent to RT turbulence, the horizontal velocity spectra are somewhat flatter than the both the vertical spectra and the $-5/3$ law in the inertial range.

Further differences between the vertical and horizontal spectra are illustrated by the anisotropy spectrum,

$$B = \frac{E_{11}^{2\text{-D}}}{E_{11}^{2\text{-D}} + E_{22}^{2\text{-D}} + E_{33}^{2\text{-D}}} - \frac{1}{3}, \tag{6.8}$$

in figure 19. This metric varies in absolute magnitude from zero for a fully isotropic velocity field to $2/3$ for a unidirectional field. The anisotropy of the HBT spectra remains within the fluctuations of the TRT spectra at almost all wavenumbers, with only one overpredicted value at the lowest HBT wavenumber and slight underpredictions at the very largest wavenumbers. Both HBT and TRT exhibit a trend of decreasing anisotropy in the energy-containing range and lower end of the inertial subrange, a minimum towards the higher end of the inertial subrange, then a gradual rise in anisotropy in the viscous range before dropping again beyond $\kappa\eta = 1$. The ability of HBT to capture this trend further validates its fidelity to the TRT turbulence structure across all length scales, including the small-scale anisotropy that characterizes buoyant turbulence. Additionally, the large statistical fluctuations in the TRT anisotropy spectrum have been heavily mitigated in HBT as a consequence of time and spatial averaging.

The velocity and anisotropy spectra also shed some light on the results of § 6.2. The strong collapse of spectra at large wavenumbers is consistent with the accurate prediction of velocity gradients in figure 17(*b*). At the same time, the truncation of HBT spectra at lower wavenumbers helps to explain the error in energy anisotropy in figure 17(*a*). Since HBT does not include the largest energy-containing length scales of TRT, which figure 19 shows are relatively isotropic, it is not surprising that the total HBT energy is more anisotropic than TRT.

The density spectra, representing contributions to the density variance at different length scales, are shown in figure 20. The TRT and HBT spectra collapse within statistical uncertainty for nearly all wavenumbers. The only possible exception is at the smallest HBT wavenumber. The strong correspondence shows that the HBT density field, having already demonstrated the statistical character of TRT in § 6.1, reproduces its spatial structure as well.

Both density spectra are slightly flatter in the inertial subrange than the $5/3$ law predicted by Obukhov (1949) and Corrsin (1951) for a passive scalar spectrum. A similar phenomenon was observed by Sreenivasan (1996) in flattened passive scalar spectra and flattened transverse velocity spectra in shear turbulent flows, where both were explained as a low-Reynolds number effect. It is possible then that the horizontal velocity and density spectra for TRT and HBT would more closely follow the expected scalings at higher Reynolds numbers.

Since the TRT $E_{11}^{2\text{-D}}$ and $E_{\rho\rho}^{2\text{-D}}$ are reproduced by HBT in the viscous range, the error in $E_{\rho 1}^{2\text{-D}}$ in the viscous range must be accompanied by an error in

$$r_{\rho 1} = \frac{E_{\rho 1}^{2\text{-D}}}{\sqrt{E_{\rho\rho}^{2D} E_{11}^{2\text{-D}}}}, \tag{6.9}$$

https://doi.org/10.1017/jfm.2026.11779 Published online by Cambridge University Press

the spectral coherence between ρ and u_1. To further compare HBT's buoyant production with that of TRT, $r_{\rho 1}$ is shown in figure 22 for HBT, alongside an approximate range of fluctuations for TRT. The HBT correlation remains within the TRT fluctuations across nearly the full range of wavenumbers, where significant underpredictions are limited to the final few wavenumbers. Both cases show a fall in correlation across the energy-containing range and much of the inertial subrange, before flattening out at the start of the viscous range. Only HBT predicts a second drop in correlation, though this is limited to a small region at the end of the viscous range. More importantly, both cases predict that some degree of correlation is preserved throughout the viscous range, so that the density and vertical velocity remain statistically dependent even at the smallest scales of turbulence. This is consistent with the argument of Livescu *et al.* (2009), reiterated by Chung & Pullin (2010), that the small-scale anisotropy of buoyant flows arises from the persistent activity of buoyant production at the small scales, which avoids domination by viscous and inertial activity due to cancellation between the dissipation and convective transport. Figure 22 also demonstrates again HBT's success in mitigating statistical fluctuations via time and space averaging.

7. Discussion

7.1. *Computational benefits*

The HBT configuration introduces vast improvements in computational efficiency over the standard RT DNS. These stem from desirable numerical properties including the following.

(i) Reduced simulation time. To obtain data at the desired Reynolds number, a TRT must be run all the way from the initially perturbed interface to the final layer height, with all the low-*Re* flow inbetween. An HBT flow, no matter the Reynolds number, requires only a few τ_t of simulation time before the initial conditions are forgotten and data can be collected.

(ii) Reduced domain size. The computational grid of the Cabot & Cook (2006) TRT DNS reaches a maximum size of 3078^3 cells, using $\kappa_{max}\eta \approx 3.14$. The HBT C31 cases has a computational grid of 448^3 cells at $\kappa_{max}\eta = 2.77$. Assuming that a common Courant–Friedrichs–Lewy condition is used, the computational speedup from the TRT to HBT for a given span of simulation time, while correcting for the difference in $\kappa_{max}\eta$ and Re_t^* (or $Re^t|_{x_1=0}$ for TRT), is given by

$$\left[\left(\frac{N^{TRT}}{N^{HBT}}\right)\frac{(\kappa_{max}\eta)^{HBT}}{(\kappa_{max}\eta)^{TRT}}\right]^4\left(\frac{Re_t^{*HBT}}{Re^t|_{x_1=0}^{TRT}}\right)^3 = \left[\left(\frac{3072}{448}\right)\frac{2.77}{3.14}\right]^4\left(\frac{3360}{3690}\right)^3 \approx 1010. \tag{7.1}$$

This is accompanied by a factor of memory savings equal to $1010^{3/4} \approx 180$.
Of course, these computational savings are obtained at the cost of the larger scales of the turbulence layer not represented by HBT. Nonetheless, if the small scales of midplane turbulence are the only information of interest, HBT can produce statistics on these scales far more efficiently than TRT.

(iii) Stationarity and homogeneity. Because TRT evolves in time and is vertically inhomogeneous, statistics can only be measured over a small window of time at a single horizontal plane, with further data requiring additional realizations. Meanwhile, in the statistically stationary and three-dimensional homogeneous HBT,

https://doi.org/10.1017/jfm.2026.11779 Published online by Cambridge University Press

the entire spatial domain of every time step contributes to measurement. This accelerates the convergence of statistics, requiring less simulation time to obtain statistics within a given tolerance of uncertainty.

Some computational cost is introduced to the framework when evaluating the mean gradient term and the layer growth term at each subiteration of each time step. However, the increase in computational time accounts for less than 1 % of total cost.

7.2. *Future work: model development*

The HBT models TRT from the Kolmogorov length scale up to a limiting length scale determined by the validity of the three assumptions listed in § 2.4. However, judging from the spectral comparison of § 6.3, only the very largest length scales appear to be subject to these errors. Although the assumptions include proximity in space to the midplane of the TRT, in § 6.2 it was found that the TRT velocity-gradient anisotropy, which HBT replicates, is nearly constant across a large range of the vertical coordinate. These facts suggest that there is some universal character to the small scales of TRT turbulence, in line with the Kolmogorov hypothesis, and that HBT is able to model a large enough range of length scales to capture this character.

This, in conjunction with the computational properties listed above, makes HBT an ideal candidate for an *a priori* and *a posteriori* test bed for buoyant turbulence SGS models. For example, the scalings in (5.6) and the data in figures 12 and 13 can be used as an *a priori* check on whether the SGS model predicts the same relationships. The model can then be implemented in LES of the HBT itself and compared with DNS results *a posteriori* as a form of early, inexpensive design iteration. This is analogous to HIT's role in the development of classical SGS models (Domaradzki, Liu & Brachet 1993; Meneveau, Lund & Cabot 1996; Meneveau & Lund 1997; Fureby *et al.* 1997; Misra & Pullin 1997; Borue & Orszag 1998; Anderson & Meneveau 1999; Langford & Moser 1999). Unlike HIT, however, HBT can account for flow anisotropy and density variation.

8. Conclusion

Applying a method originally used to model turbulence at the centreline of a jet, a new simulation framework, HBT, is developed to model the small scales of turbulence near the midplane of a TRT. This is accomplished using a set of coordinate transformations previously used to produce a statistically stationary RT instability, and adding to them a set of variable transformations that statistically homogenize the flow variables at the TRT midplane. These are substituted into the governing equations, alongside a set of assumptions regarding the proximity of the flow to the midplane. Terms with negligible contributions to the scalar variance and kinetic energy budgets are removed, and the new equations are solved in a triply periodic box domain.

A modification is applied to the source terms to damp large time fluctuations. After verifying stationarity and other numerical properties, the relationship between non-dimensional statistics and flow inputs is quantified. A comparison is then made between the Cabot & Cook (2006) TRT DNS and analogous HBT cases. The HBT framework succeeds in reproducing density and scalar PDFs at the midplane, and it predicts the anisotropy of the velocity gradient tensor across a wide range of the vertical coordinate. The framework also approximates the anisotropy of the kinetic energy within 17 %. The turbulence spectra for HBT and TRT collapse, except for errors at the lowest HBT wavenumber and small deviations in the dissipative range for the density–vertical velocity cospectrum. Small-scale anisotropy in the velocity spectra of TRT is reproduced in HBT.

https://doi.org/10.1017/jfm.2026.11779 Published online by Cambridge University Press

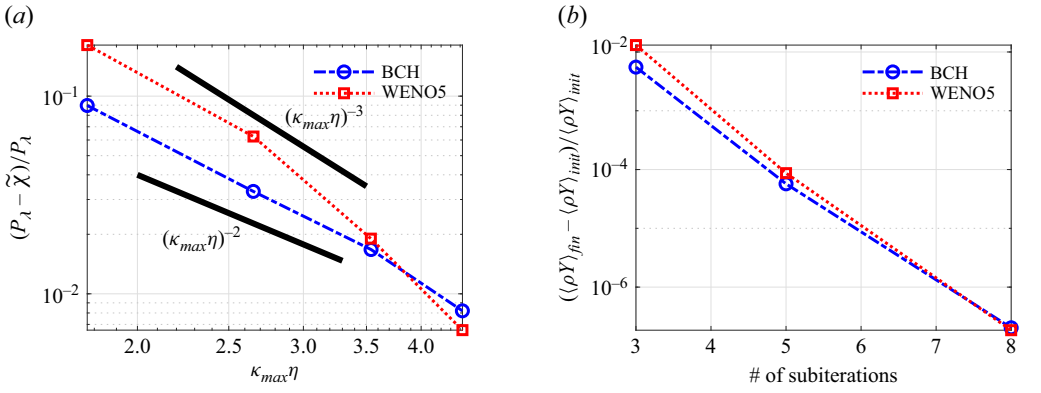


Figure 23. Quantification of (*a*) numerical diffusion for cases K1–4 and WK1–4 and (*b*) global scalar mass conservation error over $40\tau_t$ for cases S1–3 and WS1–3.

Compared with the canonical TRT, HBT is vastly more computationally affordable, having a smaller domain and transient period while allowing temporal and spatial averaging in three homogeneous directions. This makes the framework useful as a testbed for buoyant turbulence SGS models.

Acknowledgements. The authors acknowledge the Texas Advanced Computing Center (TACC) at The University of Texas at Austin for providing computational resources that have contributed to the research results reported within this paper (http://www.tacc.utexas.edu). This research used resources of the National Energy Research Scientific Computing Center (NERSC), a Department of Energy User Facility (project m4824-2024)

Funding. This material is based upon work supported by the National Science Foundation under grant no. 2422513 and the National Science Foundation Graduate Research Fellowship Program under grant no. 2139433. Any opinions, findings and conclusions or recommendations expressed in this material are those of the author(s) and do not necessarily reflect the views of the National Science Foundation.

Declaration of interests. The authors report no conflict of interest.

Appendix A. Grid sensitivity and mass conservation

In choosing a scalar scheme for the present study, four properties are considered:

(i) boundedness;
(ii) high numerical accuracy;
(iii) low numerical dissipation;
(iv) conservation

The scalar schemes WENO5 (an Eulerian scheme) and BCH (a semi-Lagrangian scheme) are both bounded and have reasonably high orders of accuracy. The choice between the two is then a trade-off between low numerical dissipation (BCH) and mass conservation (WENO5).

To guide the selection of scalar scheme, assess grid-sensitivity and optimize numerical parameters, HBT cases were run with both BCH and WENO5 at different grid resolutions and numbers of subiterations in the time-integration scheme. The inputs and some statistics for these cases are given in table 4. Statistics are calculated from time-series data over a period of $100\tau_t$.

Figure 23(*a*) shows the relative difference between the scalar variance injection rate and the Favre average of scalar dissipation rate for four different grid resolutions, measured by

https://doi.org/10.1017/jfm.2026.11779 Published online by Cambridge University Press

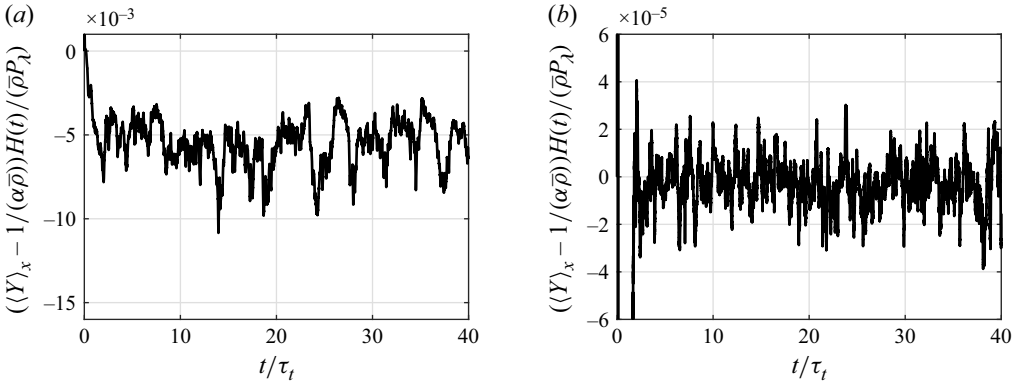


Figure 24. Scalar variance source over time arising from the scalar conservation correction, for (*a*) case R3/A4 and (*b*) case A1.

$\kappa_{max}\eta^*$. Recall from (3.14) that, in a stationary state, the two values should be equal in a perfectly resolved simulation. Thus, the relative discrepancy between the two represents the numerical dissipation as a fraction to the total dissipation. Results for both the WENO5 and BCH scalar schemes are shown. Based on the fiducials shown, both schemes exhibit their expected orders of accuracy: second order for BCH and third order for WENO5. For all grid sizes, BCH produces less numerical dissipation than WENO5. While the numerical dissipation for BCH is $\approx 4\,\%$ at $\kappa_{max}\eta^* \approx 2.4$, WENO5 does not achieve the same degree of accuracy until $\kappa_{max}\eta^* \approx 2.9$. A 4 % numerical dissipation is considered sufficiently low for this study, so the BCH scheme is used throughout at $k_{max}\eta^* = 2.4$.

Figure 23(*b*) gives the relative change in volume-average scalar mass $\langle \rho Y\rangle$ from $t = 0$ to $t = 40\tau_t$. Since the volume-averaged scalar mass is a conserved quantity (the volume average of the source term in scalar transport (2.48) is zero), this represents an error in primary conservation. As noted in § 4.1, large conservation errors are characteristic of the BCH scheme but have been mitigated with a spatially uniform correction at each time step. The remaining conservation error, for both schemes, arises from failure of the iterative time-integration to converge fully to the implicit midpoint scheme. From figure 23(*b*), the error decreases exponentially with each subiteration for both schemes. The BCH scheme produces slightly smaller error than WENO5, and at five subiterations the relative change in scalar mass for BCH is only $\approx 6 \times 10^{-5}$. Therefore, five subiterations are used for all other HBT cases.

To quantify the impact of the conservation correction on the scalar variance budget, we first write out the scalar transport equation for HBT,

$$\frac{\partial \rho Y}{\partial t} = \mathrm{RHS} + H(t), \tag{A1}$$

where RHS includes all physical convection, diffusion and source terms, while $H(t)$ is the correction that guarantees global conservation. The density-weighted scalar variance transport equation is then

$$\frac{\partial \overline{\rho}\widetilde{Y''^2}}{\partial t} = \overline{Y''\mathrm{RHS}} + \overline{Y''H(t)}. \tag{A2}$$

The source of variance arising from $H(t)$, $\overline{Y''H(t)}$, can be estimated as $[\langle Y\rangle_x - 1/(\alpha\overline{\rho})]H(t)$. This quantity is plotted against time in figure 24(*a*) for case R3/A4, normalized by the product of Reynolds-average density and mean gradient production, $\overline{\rho}P_\lambda$. The

https://doi.org/10.1017/jfm.2026.11779 Published online by Cambridge University Press

Case	$\kappa_{max}\eta^*$	$\frac{\widetilde{k^*}}{(P_g L)^{2/3}}$	$\frac{\widetilde{Y^{*\prime\prime}2}}{P_A P_g^{1/3} L^{2/3}}$	Re_t^*	At_{eff}^*
K1	1.77	0.502 ± 0.009	0.215 ± 0.004	312 ± 10	0.272 ± 0.003
K2	2.65	0.487 ± 0.008	0.209 ± 0.004	298 ± 8	0.266 ± 0.003
K3	3.54	0.500 ± 0.012	0.216 ± 0.005	309 ± 13	0.273 ± 0.004
K4	4.43	0.512 ± 0.018	0.221 ± 0.008	322 ± 18	0.274 ± 0.005
WK1	1.77	0.500 ± 0.012	0.210 ± 0.005	311 ± 12	0.270 ± 0.004
WK2	2.65	0.504 ± 0.011	0.217 ± 0.005	315 ± 9	0.271 ± 0.003
WK3	3.54	0.481 ± 0.008	0.208 ± 0.003	291 ± 8	0.267 ± 0.003
WK4	4.42	0.485 ± 0.009	0.211 ± 0.004	296 ± 10	0.267 ± 0.003

Table 6. Effect of grid resolution and scalar scheme on HBT statistics.

contribution of the correction to the scalar budget is less than 1 % of the variance production, which is negligible compared with numerical dissipation. To ensure that the contribution of the correction does not dominate when the mean gradient production is small, the same quantity is plotted for case A1 in figure 24(*b*). After an initial transient, the relative contribution is more than two orders of magnitude lower than in the R3/A4 case. The contribution remains negligible within the parameter space examined in this study.

Table 6 gives the values and uncertainties of statistics across grid resolutions for BCH and WENO5 cases. These include the kinetic energy, density-weighted scalar variance (both normalized by HBT input parameters), Re_t^*, and At_{eff}^*. Uncertainties are calculated from time-series data using the method described in Rah & Blanquart (2019). For each statistic, the ranges of uncertainty touch or overlap across all four resolutions and between the two scalar schemes. The statistics are therefore insensitive to the grid-resolution within the studied range of $\kappa_{max}\eta^*$. Furthermore, the use of a non-conservative scheme like BCH with a spatially uniform correction, as opposed to a conservative scheme like WENO5, does not meaningfully affect these statistics.

Appendix B. Scalar and density extrema in HBT

Unlike TRT and SRT, HBT does not impose boundaries on the scalar as inputs to the configuration. As such, the extrema of the scalar and density are output statistics of the system rather than input parameters.

To examine the relationship between the density/scalar extrema and At_{eff}, the maximum and minimum values of ρ and Y (across space for a given time snapshot) are plotted against time in figure 25(*a*,*b*) for HBT cases A1–5. While the maxima increase and minima decrease relative to the mean value as At_{eff} is increased, neither ρ nor Y ever reach zero or become unbounded.

Figure 26(*a*,*b*) shows the minima and maxima time series at different grid resolutions. As $\kappa_{max}\eta$ is increased from 1.77 to 4.43, the time-series remain indistinguishable from each other. Therefore, while density and scalar extrema are not directly imposed in HBT, density and scalar fields are physically bounded, and these bounds may be controlled via physical HBT input parameters.

Appendix C. Calculation of spectral budgets

To obtain the spectral kinetic energy budget for midplane SRT, we take the 2-D Fourier transform of the advective form of the momentum equation:

https://doi.org/10.1017/jfm.2026.11779 Published online by Cambridge University Press

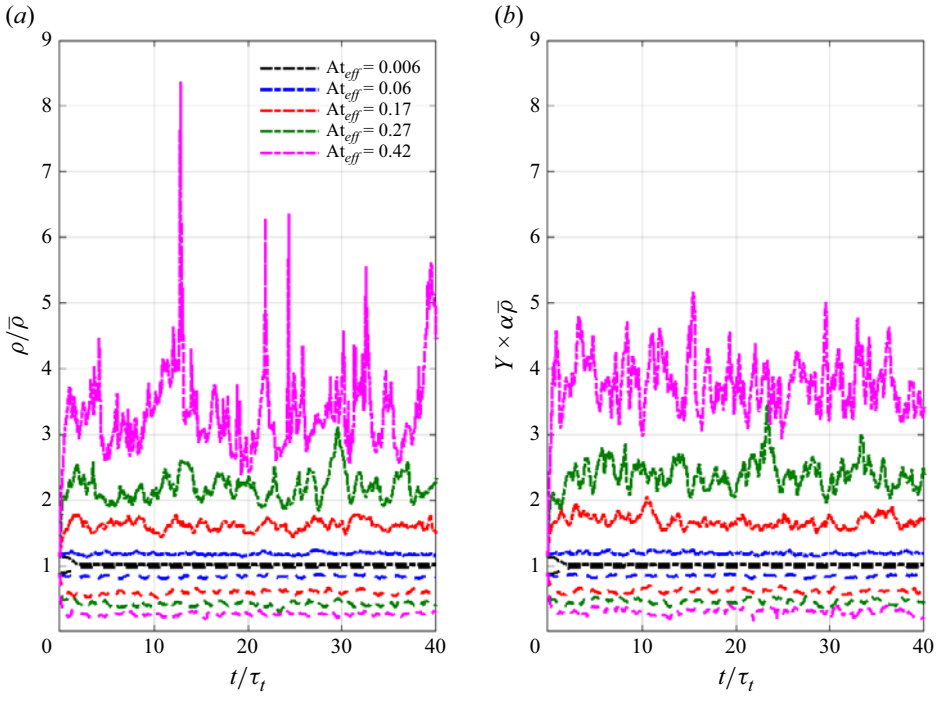


Figure 25. Minimum (dashed) and maximum (dot–dashed) values of (*a*) density and (*b*) scalar versus time, for HBT cases A1–5.

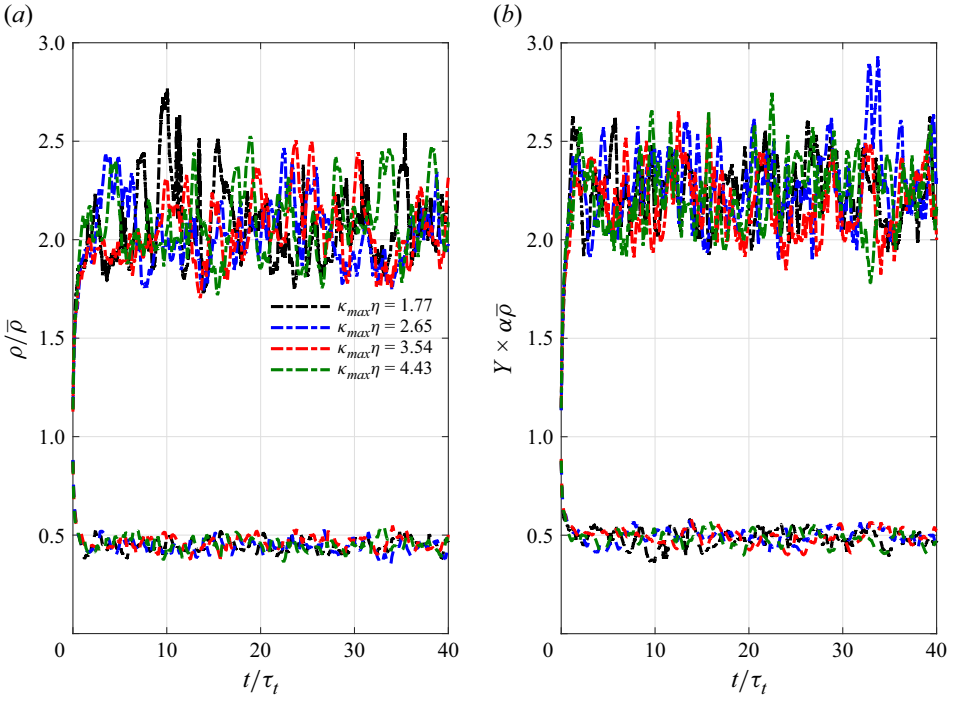


Figure 26. Minimum (dashed) and maximum (dot–dashed) values of (*a*) density and (*b*) scalar versus time, for HBT cases K1–4.

https://doi.org/10.1017/jfm.2026.11779 Published online by Cambridge University Press

$$\frac{\partial \mathscr{F}^{2\text{-D}}\{u_i\}}{\partial t} + \mathscr{F}^{2\text{-D}}\left\{u_j \frac{\partial u_i}{\partial x_j}\right\} = -\mathscr{F}^{2\text{-D}}\left\{\frac{1}{\rho}\frac{\partial p}{\partial x_i}\right\} + \mathscr{F}^{2\text{-D}}\left\{\frac{1}{\rho}\frac{\partial \tau_{ij}}{\partial x_j}\right\} + g\mathscr{F}^{2\text{-D}}\left\{\left(1-\frac{\overline{\rho}}{\rho}\right)\delta_{i1}\right\} - \mathscr{F}^{2\text{-D}}\left\{\frac{1}{\rho}\frac{1}{2\tau_o}\rho u_i\right\}. \tag{C1}$$

This is multiplied by the conjugate of the Fourier transform of u_i', the real part is taken, and the result is integrated around annuli in wavevector space. In practice, binning is used, where averages of κ and the integrand are taken within uniform bins of wavenumber magnitude, then the average integrand is multiplied by the average κ times 2π to estimate the integral over θ,

$$\begin{aligned}\frac{1}{2}\frac{\partial E_{11}^{2\text{-D}}}{\partial t} + \int_0^{2\pi} \mathrm{Re}\left(\mathscr{F}^{2\text{-D}^*}\left\{u_i'\right\}\mathscr{F}^{2\text{-D}}\left\{u_j\frac{\partial u_i}{\partial x_j}\right\}\right)\kappa\,\mathrm{d}\theta &= -\int_0^{2\pi} \mathrm{Re}\left(\mathscr{F}^{2\text{-D}^*}\left\{u_i'\right\}\mathscr{F}^{2\text{-D}}\left\{\frac{1}{\rho}\frac{\partial p}{\partial x_i}\right\}\right)\kappa\,\mathrm{d}\theta \\ &+ \int_0^{2\pi} \mathrm{Re}\left(\mathscr{F}^{2\text{-D}^*}\left\{u_i'\right\}\mathscr{F}^{2\text{-D}}\left\{\frac{1}{\rho}\frac{\partial \tau_{ij}}{\partial x_j}\right\}\right)\kappa\,\mathrm{d}\theta \\ &+ g\int_0^{2\pi} \mathrm{Re}\left(\mathscr{F}^{2\text{-D}^*}\left\{u_i'\right\}\mathscr{F}^{2\text{-D}}\left\{\left(1-\frac{\overline{\rho}}{\rho}\right)\delta_{i1}\right\}\right)\kappa\,\mathrm{d}\theta \\ &- \int_0^{2\pi} \mathrm{Re}\left(\mathscr{F}^{2\text{-D}^*}\left\{u_i'\right\}\mathscr{F}^{2\text{-D}}\left\{\frac{1}{\rho}\frac{1}{2\tau_o}\rho u_i\right\}\right)\kappa\,\mathrm{d}\theta,\end{aligned} \tag{C2}$$

where product rule and the definition of the 2-D spectrum (6.4) was used to obtain the time derivative of the energy spectrum. The remaining terms represent the contributions by convection, pressure, viscous effects, buoyant production and layer growth, respectively. The process is the same for HBT, only the variables are replaced with their transformed variants and the gravity term is replaced by the modified term of (3.12):

$$\frac{\overline{\rho^*}P_g}{|\langle\rho^{*'}u_1^{*'}\rangle|}\int_0^{2\pi} \mathrm{Re}\left(\mathscr{F}^{2\text{-D}^*}\left\{u_i^{*'}\right\}\mathscr{F}^{2\text{-D}}\left\{\frac{\rho^{*'}}{\rho^*}\delta_{i1}\right\}\right)\kappa\,\mathrm{d}\theta. \tag{C3}$$

For the scalar variance budget in SRT, the mean gradient production is separated from convection in the advective form of the scalar equation:

$$\frac{\partial Y}{\partial t} + \left(u_j\frac{\partial Y}{\partial x_j} + \frac{1}{\rho}\frac{u_1'}{\alpha\lambda_o}\right) = \frac{1}{\rho}\frac{\partial}{\partial x_j}\left(D\rho\frac{\partial Y}{\partial x_j}\right) + \frac{1}{\rho}\frac{u_1'}{\alpha\lambda_o}. \tag{C4}$$

The Fourier transform is taken, multiplied by the conjugate of the Fourier transform of Y', and integrated as before,

$$\begin{aligned}\frac{\partial E_{YY}^{2\text{-D}}}{\partial t} + \int_0^{2\pi} \mathrm{Re}\left(\mathscr{F}^{2\text{-D}^*}\left\{Y'\right\}\mathscr{F}^{2\text{-D}}\left\{\left(u_j\frac{\partial Y}{\partial x_j} + \frac{1}{\rho}\frac{u_1'}{\alpha\lambda_o}\right)\right\}\right)\kappa\,\mathrm{d}\theta &= \int_0^{2\pi} \mathrm{Re}\left(\mathscr{F}^{2\text{-D}^*}\left\{Y'\right\}\mathscr{F}^{2\text{-D}}\left\{\frac{1}{\rho}\frac{\partial}{\partial x_j}\left(D\rho\frac{\partial Y}{\partial x_j}\right)\right\}\right)\kappa\,\mathrm{d}\theta \\ &+ \frac{1}{\alpha\lambda_o}\int_0^{2\pi} \mathrm{Re}\left(\mathscr{F}^{2\text{-D}^*}\left\{Y'\right\}\mathscr{F}^{2\text{-D}}\left\{\frac{u_1'}{\rho}\right\}\right)\kappa\,\mathrm{d}\theta.\end{aligned} \tag{C5}$$

https://doi.org/10.1017/jfm.2026.11779 Published online by Cambridge University Press

After the time derivative, the terms represent convection, diffusion and mean gradient production, respectively. In HBT, the variables are replaced by their transformed variants, the mean gradient production is no longer subtracted from the convection term (it is implicitly removed by the transformations), and the mean gradient production is replaced by the modification of (3.12):

$$\begin{aligned}\frac{\partial E_{YY}^{2\text{-D}}}{\partial t} &+ \int_0^{2\pi} \mathrm{Re}\left(\mathscr{F}^{2\text{-D}^*}\left\{Y^{*'}\right\}\mathscr{F}^{2\text{-D}}\left\{u_j^*\frac{\partial Y^*}{\partial x_j}\right\}\right)\kappa\,\mathrm{d}\theta \\ &= \int_0^{2\pi} \mathrm{Re}\left(\mathscr{F}^{2\text{-D}^*}\left\{Y^{*'}\right\}\mathscr{F}^{2\text{-D}}\left\{\frac{1}{\rho^*}\frac{\partial}{\partial x_j}\left(D\rho^*\frac{\partial Y^*}{\partial x_j}\right)\right\}\right)\kappa\,\mathrm{d}\theta \\ &\quad + \frac{\overline{\rho^*}P_\lambda}{|\langle u_1^{*'}Y^{*'}\rangle|}\int_0^{2\pi} \mathrm{Re}\left(\mathscr{F}^{2\text{-D}^*}\left\{Y^{*'}\right\}\mathscr{F}^{2\text{-D}}\left\{\frac{u_1^{*'}}{\rho^*}\right\}\right)\kappa\,\mathrm{d}\theta. \end{aligned} \tag{C6}$$

References

Abarzhi, S.I. 2010 Review of theoretical modelling approaches of Rayleigh–Taylor instabilities and turbulent mixing. *Phil. Trans. R. Soc. A* **368**, 1809–1828, 1916.

Addad, Y., Benhamadouche, S. & Laurence, D. 2004 The negatively buoyant wall-jet: LES results. *Intl J. Heat Fluid Flow* **25** (5), 795–808.

Anderson, R. & Meneveau, C. 1999 Effects of the similarity model in finite-difference LES of isotropic turbulence using a Lagrangian dynamic mixed model. *Flow Turbul. Combust.* **62** (3), 201–225.

Andrews, M.J. & Dalziel, S.B. 2010 Small Atwood number Rayleigh–Taylor experiments. *Phil. Trans. R. Soc. A* **368**, 1663–1679, 1916.

Banerjee, A. 2020 Rayleigh–Taylor instability: a status review of experimental designs and measurement diagnostics. *J. Fluids Engng* **142** (12), 120801.

Banerjee, A., Kraft, W.N. & Andrews, M.J. 2010 Detailed measurements of a statistically steady Rayleigh–Taylor mixing layer from small to high Atwood numbers. *J. Fluid Mech.* **659**, 127–190.

Boffetta, G. & Mazzino, A. 2017 Incompressible Rayleigh–Taylor turbulence. *Annu. Rev. Fluid Mech.* **49**, 119–143.

Boffetta, G., Mazzino, A., Musacchio, S. & Vozella, L. 2009 Kolmogorov scaling and intermittency in Rayleigh–Taylor turbulence. *Phys. Rev. E* **79** (6), 065301(R).

Borue, V. & Orszag, S.A. 1998 Local energy flux and subgrid-scale statistics in three-dimensional turbulence. *J. Fluid Mech.* **366**, 1–31.

Burton, G.C. 2009 Large-eddy simulation of a turbulent helium-air plume using the NLES method. In *Annual Research Briefs*. Stanford University, CA, Citeseer.

Cabot, W.H. & Cook, A.W. 2006 Reynolds number effects on Rayleigh–Taylor instability with possible implications for type-ia supernovae. *Nat. Phys.* **2**, 562–568.

Cabot, W.H. & Zhou, Y. 2013 Statistical measurements of scaling and anisotropy of turbulent flows induced by Rayleigh–Taylor instability. *Phys. Fluids* **25** (1), 015107.

Carroll, P.L. & Blanquart, G. 2013 A proposed modification to Lundgren's physical space velocity forcing method for isotropic turbulence. *Phys. Fluids* **25** (10), 105114.

Carroll, P.L. & Blanquart, G. 2015 A new framework for simulating forced homogeneous buoyant turbulent flows. *Theor. Comput. Fluid Dyn.* **29** (3), 225–244.

Chung, D. & Pullin, D.I. 2010 Direct numerical simulation and large-eddy simulation of stationary buoyancy-driven turbulence. *J. Fluid Mech.* **643**, 279–308.

Cook, A.W., Cabot, W.H. & Miller, P.L. 2004 The mixing transition in Rayleigh–Taylor instability. *J. Fluid Mech.* **511**, 333–362.

Corrsin, S. 1951 On the spectrum of isotropic temperature fluctuations in an isotropic turbulence. *J. Appl. Phys.* **22** (4), 469–473.

Desjardin, P.E., O'Hern, T.J. & Tieszen, S.R. 2004 Large eddy simulation and experimental measurements of the near-field of a large turbulent helium plume. *Phys. Fluids* **16** (6), 1866–1883.

Desjardins, O., Blanquart, G., Balarac, G. & Pitsch, H. 2008 High order conservative finite difference scheme for variable density low Mach number turbulent flows. *J. Comput. Phys.* **227** (15), 7125–7159.

https://doi.org/10.1017/jfm.2026.11779 Published online by Cambridge University Press

DHANDAPANI, C., RAH, K.J. & BLANQUART, G. 2019 Effective forcing for direct numerical simulations of the shear layer of turbulent free shear flows. *Phys. Rev. Fluids* **4** (8), 084606.
DIMONTE, G. & SCHNEIDER, M. 2000 Density ratio dependence of Rayleigh–Taylor mixing for sustained and impulsive acceleration histories. *Phys. Fluids* **12** (2), 304–321.
DIMONTE, G., *et al.* 2004 A comparative study of the turbulent Rayleigh–Taylor instability using high-resolution three-dimensional numerical simulations: the alpha-group collaboration. *Phys. Fluids* **16** (5), 1668–1693.
DOMARADZKI, J.A., LIU, W. & BRACHET, M.E. 1993 An analysis of subgrid-scale interactions in numerically simulated isotropic turbulence. *Phys. Fluids* **5** (7), 1747–1759.
ESWARAN, V. & POPE, S.B. 1988 Direct numerical simulations of the turbulent mixing of a passive scalar. *Phys. Fluids* **31** (3), 506–520.
FUREBY, C., TABOR, G., WELLER, H.G. & GOSMAN, A.D. 1997 A comparative study of subgrid scale models in homogeneous isotropic turbulence. *Phys. Fluids* **9** (5), 1416–1429.
GODEFERD, F.S. & CAMBON, C. 1994 Detailed investigation of energy transfers in homogeneous stratified turbulence. *Phys. Fluids* **6** (6), 2084–2100.
GOH, C.Y. & BLANQUART, G. 2025 A statistically stationary minimal flow unit for self-similar Rayleigh–Taylor turbulence in the mode-coupling limit. *J. Fluid Mech.* **1002**, A19.
GOH, C.Y., MATEHUALA, B., Daniel, & BLANQUART, G. 2026 Self-similar scaling of variable-density Rayleigh–Taylor turbulence. *J. Fluid Mech.* **1030**, A14.
GRIFFOND, J., GRÉA, B.J. & SOULARD, O. 2014 Unstably stratified homogeneous turbulence as a tool for turbulent mixing modeling. *J. Fluids Engng* **136** (9), 091201.
LANGFORD, J.A. & MOSER, R.D. 1999 Optimal LES formulations for isotropic turbulence. *J. Fluid Mech.* **398**, 321–346.
LIVESCU, D. & RISTORCELLI, J.R. 2008 Variable-density mixing in buoyancy-driven turbulence. *J. Fluid Mech.* **605**, 145–180.
LIVESCU, D., RISTORCELLI, J.R., GORE, R.A., DEAN, S.H., CABOT, W.H. & COOK, A.W. 2009 High-Reynolds number Rayleigh—Taylor turbulence. *J. Turbul.* **10**, N13.
LIVESCU, D. & RISTORCELLI, J.R. 2007 Buoyancy-driven variable-density turbulence. *J. Fluid Mech.* **591**, 43–71.
LIVESCU, D., RISTORCELLI, J.R., PETERSEN, M.R. & GORE, R.A. 2010 New phenomena in variable-density Rayleigh–Taylor turbulence. *Phys. Scripta* **T142**, 014015.
LIVESCU, D., WEI, T. & PETERSEN, M.R. 2011 Direct numerical simulations of Rayleigh–Taylor instability. *J. Phys. Conf. Ser.* **318**, 082007.
LUMLEY, J.L. 1967 Similarity and the turbulent energy spectrum. *Phys. Fluids* **10** (4), 855–858.
LUNDGREN, T.S. 2003 Linearly forced isotropic turbulence. In *Center for Turbulence Research Annual Research Briefs*, pp. 461–473.
LUO, T., WANG, Y., YUAN, Z., JIANG, Z., HUANG, W. & WANG, J. 2023 Large-eddy simulations of compressible Rayleigh–Taylor turbulence with miscible fluids using spatial gradient model. *Phys. Fluids* **35** (10), 105131.
MAZZINO, A. 2017 Two-dimensional turbulent convection. *Phys. Fluids* **29** (11), 111102.
MELLADO, J.P., SARKAR, S. & ZHOU, Y. 2005 Large-eddy simulation of Rayleigh–Taylor turbulence with compressible miscible fluids. *Phys. Fluids* **17** (7), 076101.
MENEVEAU, C. & LUND, T.S. 1997 The dynamic Smagorinsky model and scale-dependent coefficients in the viscous range of turbulence. *Phys. Fluids* **9** (12), 3932–3934.
MENEVEAU, C., LUND, T.S. & CABOT, W.H. 1996 A Lagrangian dynamic subgrid-scale model of turbulence. *J. Fluid Mech.* **319**, 353–385.
MISRA, A. & PULLIN, D.I. 1997 A vortex-based subgrid stress model for large-eddy simulation. *Phys. Fluids* **9** (8), 2443–2454.
OBUKHOV, A.M. 1949 Structure of temperature field in turbulent flow. *Izvestiya Akademiya Nauk SSSR* **13**, 58–69.
OVERHOLT, M.R. & POPE, S.B. 1998 A deterministic forcing scheme for direct numerical simulations of turbulence. *Comput. Fluids* **27** (1), 11–28.
POPE, S.B. 2001 *Turbulent Flows*. IOP Publishing.
RAH, K.J. & BLANQUART, G. 2019 Numerical forcing scheme to generate passive scalar mixing on the centerline of turbulent round jets in a triply periodic box. *Phys. Rev. Fluids* **4** (12), 124504.
RAH, K.J., DHANDAPANI, C. & BLANQUART, G. 2018 Derivation of a realistic forcing term to reproduce the turbulent characteristics of round jets on the centerline. *Phys. Rev. Fluids* **3** (8), 084606.
RAMAPRABHU, P. & ANDREWS, M.J. 2004 Experimental investigation of Rayleigh–Taylor mixing at small Atwood numbers. *J. Fluid Mech.* **502**, 233–271.

https://doi.org/10.1017/jfm.2026.11779 Published online by Cambridge University Press

RAYLEIGH, Lord 1882 Investigation of the character of the equilibrium of an incompressible heavy fluid of variable density. *Proc. R. Soc.* **14** (1), 170–177.

RISTORCELLI, J.R. & CLARK, T.T. 2004 Rayleigh–Taylor turbulence: self-similar analysis and direct numerical simulations. *J. Fluid Mech.* **507**, 213–253.

ROSALES, C. & Meneveau. Charles 2005 Linear forcing in numerical simulations of isotropic turbulence: physical space implementations and convergence properties. *Phys. Fluids* **17** (9), 095106.

SCHILLING, O. 2020 Progress on understanding Rayleigh–Taylor flow and mixing using synergy between simulation, modeling, and experiment. *J. Fluids Engng* **142** (12), 120802.

SOULARD, O., GRIFFOND, JÉROME & GRÉA, B.ÎT-J. 2014 Large-scale analysis of self-similar unstably stratified homogeneous turbulence. *Phys. Fluids* **26** (1), 015110.

SREENIVASAN, K.R. 1996 The passive scalar spectrum and the Obukhov–Corrsin constant. *Phys. Fluids* **8** (1), 189–196.

TAYLOR, G.I. 1950 The instability of liquid surfaces when accelerated in a direction perpendicular to their planes. *I. Proc. R. Soc. Lond. A* **201** (1065), 192–196.

TIESZEN, S.R., O'HERN, T.J., SCHEFER, R.W., WECKMAN, E.J. & BLANCHAT, T.K. 2002 Experimental study of the flow field in and around a one meter diameter methane fire. *Combust. Flame* **129** (4), 378–391.

VERMA, S., XUAN, Y. & BLANQUART, G. 2014 An improved bounded semi-Lagrangian scheme for the turbulent transport of passive scalars. *J. Comput. Phys.* **272**, 1–22.

VLADIMIROVA, N. & CHERTKOV, M. 2009 Self-similarity and universality in Rayleigh–Taylor, Boussinesq turbulence. *Phys. Fluids* **21** (1), 015102.

XU, Z. & Shu Chi-wang 2005 Anti-diffusive flux corrections for high order finite difference WENO schemes. *J. Comput. Phys.* **205** (2), 458–485.

YILMAZ, I. 2020 Analysis of Rayleigh–Taylor instability at high Atwood numbers using fully implicit, non-dissipative, energy-conserving large eddy simulation algorithm. *Phys. Fluids* **32** (5), 054101.

YOUNGS, D.L. 1984 Numerical simulation of turbulent mixing by Rayleigh–Taylor instability. *Physica D* **12** (1–3), 32–44.

YOUNGS, D.L. 2013 The density ratio dependence of self-similar Rayleigh–Taylor mixing. *Phil. Trans. R. Soc. A* **371**, 201201732003.

ZHOU, Y. 2001 A scaling analysis of turbulent flows driven by Rayleigh–Taylor and Richtmyer–Meshkov instabilities. *Phys. Fluids* **13** (2), 538–543.

ZHOU, Y. 2017*a* Rayleigh–Taylor and Richtmyer–Meshkov instability induced flow, turbulence, and mixing. *I. Phys. Rep.* **720**, 1–125.

ZHOU, Y. 2017*b* Rayleigh–Taylor and Richtmyer–Meshkov instability induced flow, turbulence, and mixing. *II. Phys. Rep.* **723**, 1–160.

ZHOU, Y. & CABOT, W.H. 2019 Time-dependent study of anisotropy in Rayleigh–Taylor instability induced turbulent flows with a variety of density ratios. *Phys. Fluids* **31** (8), 084106.

https://doi.org/10.1017/jfm.2026.11779 Published online by Cambridge University Press